Time-resolved phenotyping at subcellular resolution reveals shared principles and key trade-offs across antimicrobial peptide activities

Alessio Fragasso[1-3], Tatjana Schlechtweg[1,3], Wei-Hsiang Lin[1,3,#], Annelise E. Barron[4], and Christine Jacobs-Wagner[1-5,*]

[1]Sarafan ChEM-H Institute, Stanford University, Stanford, CA, USA

[2]Department of Biology, Stanford University, Stanford, CA, USA

[3]Howard Hughes Medical Institute, Stanford University, Stanford, CA, USA

[4]Department of Bioengineering, Stanford University, Schools of Medicine and of Engineering, Stanford, CA, USA

[5]Department of Microbiology and Immunology, Stanford University, School of Medicine, Stanford, CA, USA

[#]Current address: Institute of Molecular Biology, Academia Sinica, Taipei, Taiwan

[*]Corresponding author (jacobs-wagner@stanford.edu)

ABSTRACT

Cationic antimicrobial peptides are a large family of host defense molecules with diverse sequences and structures. Here, we present a computational and experimental pipeline for time-resolved quantification of both membrane-permeabilizing and intracellular effects in *Escherichia coli*. Applying this pipeline to 12 diverse natural peptides and synthetic peptidomimetics uncovers shared antimicrobial activities, but with different kinetics, forming two classes. With class I peptides, growth arrest is abrupt and predominantly coupled with inner membrane permeabilization and ribosome/DNA reorganization. However, membrane permeabilization leads to rapid peptide absorption by the first exposed bacterial cells, resulting in low efficacy against dense populations. With class II peptides, ribosome/DNA reorganization and growth inhibition occur more gradually, as inner membrane permeabilization is either absent or delayed. This is offset by slower intracellular peptide uptake and greater efficacy against high cell densities. These kinetic differences reveal functional trade-offs between classes that have major immunological and therapeutic implications.

INTRODUCTION

Antimicrobial peptides (AMPs) are a large group of host defense peptides produced by virtually all organisms, ranging from bacteria to plants and animals, including humans (Wang et al., 2016, 2022). These naturally occurring peptides have garnered significant interest due to their multimodal role in innate immunity, where they serve as both antimicrobial agents and immunomodulators (Hancock et al., 2016; Mookherjee et al., 2020). Furthermore, their broad-spectrum efficacy against bacteria, viruses, fungi, and parasites, coupled with a low tendency for resistance development, have made them attractive candidates for antibiotic alternatives or supplements (Mookherjee et al., 2020; Taheri-Araghi, 2024). Consequently, significant efforts have been dedicated to developing synthetic AMPs and peptidomimetics to combat the threat of infectious diseases and the rise of antibiotic resistance.

With over 2,500 natural AMPs identified in animals alone (as of December 2024), the sheer diversity of peptide sequence is remarkable (Wang et al., 2016). They also vary in structure, encompassing α-helical forms, β-sheets, β-hairpins, and extended structures. Moreover, some AMPs undergo post-translational modifications (Wang et al., 2016), further contributing to their diversity. Notwithstanding their structural differences, many AMPs share two key physicochemical features: they are typically amphipathic and cationic (at physiological pH). These properties enable AMPs to interact with bacterial cytoplasmic membranes, which are negatively charged in part due to the prevalence of anionic phospholipids. Gram-negative bacteria possess an additional outer membrane typically rich in anionic lipopolysaccharides (LPS), which provides another target for cationic AMPs.

Numerous cellular targets and mechanisms of action of AMPs have been proposed, occasionally for the same peptides (Li et al., 2022; Peschel & Sahl, 2006; Wimley & Hristova, 2011). Most AMPs disrupt the integrity of bacterial membranes (Wimley & Hristova, 2011). Others, particularly proline-rich peptides, inhibit bacterial growth without reported membrane disruption (Hale & Hancock, 2007; Scocchi et al., 2011). These peptides use cellular transporters to enter the cytoplasm, where they are thought to disrupt the activity of ribosomes or DnaK, a chaperone involved in protein folding (Huang et al., 2024; Scocchi et al., 2011). Complicating the picture, different mechanisms of action have been proposed for the same peptides. For example, several membrane-disruptive peptides have been suggested to bind intracellular anionic targets such as DNA, RNAs, ribosomes, or other molecules (Cardoso et al., 2019; Luo & Song, 2021). In addition, AMPs have been reported to exert

global intracellular effects, such as cytoplasmic phase separation, aggregation, flocculation, and/or rigidification (Boeynaems et al., 2023; Chongsiriwatana et al., 2017; Sneideris et al., 2023; Zhu et al., 2019). This suggests that AMPs may exert diverse cellular effects; yet the temporal relationship between each effect and bacterial growth inhibition is often unknown. Moreover, animals—including humans—commonly produce multiple AMPs. Whether this molecular diversity enables distinct immunological strategies is unclear.

Time-lapse microscopy offers a powerful method to monitor cellular events associated with AMP activity over time at single-cell and subcellular resolution (Choi et al., 2016). In this work, we expand upon this approach experimentally and computationally to quantify membrane permeabilization and intracellular phenotypes elicited by a diverse set of cationic AMPs and peptidomimetics under the same standardized conditions. We examine their effects on both the inner and outer membranes, as well as on ribosomes and DNA in *Escherichia coli*. Our study uncovers commonalities and differences across AMP activities that reveal major trade-offs and distinct immunological strategies.

RESULTS

For our study, we selected ten natural cationic AMPs that vary widely with respect to their animal source, sequence, structure, net positive charge, and size: bactenecin-7 (Bac7), cecropin A (CecA), human β-defensin 3 (HBD-3), indolicidin (Indo), LL-37, magainin-2 (Mag2), melittin (Mltt), PR-39, tachyplesin-1 (Tac1), and Tur1A (Figure 1A-B). These peptides also vary in their grand average of hydropathy (GRAVY) index and in their fraction of lysine, arginine, proline, polar, and hydrophobic residues (Figure 1B and Table S1). Some of the selected AMPs carry modifications such as disulfide bonds or a C-terminal NH_2 group, further increasing the diversity of our panel (Figure 1A). For each peptide, we determined the minimal inhibitory concentration (MIC) for *E. coli* (strain MG1655) grown under identical growth conditions (37°C, M9 minimal medium with glucose, casamino acids, and thiamine, or M9gluCAAT), starting with a low inoculum density of cells (~250 cells/mL) (Figure S1A). For imaging, we built a simple microwell device (Figure S1B) that contains four independent wells where the growth and division of immobilized *E. coli* cells can be tracked. With this setup, AMPs can be easily added at a defined final concentration, unlike with agarose pads, which are often used for time-lapse imaging of bacterial cells. We chose this setup over popular microfluidic devices (e.g., mother machines) because it requires smaller amounts of AMP, as some of these peptides are costly or difficult to obtain (e.g., due to their chemical modifications).

AMPs are often functionally classified as 'lytic' or 'non-lytic' based on their membrane-permeabilizing activity. This activity is commonly assessed using membrane-impermeant dyes that bind to nucleic acids such as SYTOX Green (Roth et al., 1997). Unlike the selected AMPs, SYTOX Green is small enough to diffuse into the periplasmic space through OM porins. Therefore, its uptake by Gram-negative bacteria such as *E. coli* is generally assumed to examine the integrity of the IM (Roth et al., 1997). Our first aim was to determine whether the growth arrest caused by the evaluated AMPs is associated with the permeabilization of the outer membrane (OM), the inner membrane (IM), or both. To monitor the integrity of the two membranes independently, we constructed an *E. coli* strain that carries two free fluorescent proteins: the red fluorescent protein mScarlet-I in the periplasmic space (i.e., between the IM and OM) and the blue fluorescent protein mTagBFP2 in the cytoplasm (Figure 1C). The mScarlet-I signal was frequently enriched at one or both cell poles due to a larger periplasmic space at these locations (Figure S1C).

Time-lapse wide-field microscopy was initiated before the addition of an AMP to ensure that cells grew normally in its absence. Each AMP was then added to achieve a final concentration equivalent to 2X MIC (Figure 1A) to study its primary effect on cells, with the concentration slightly above the MIC to ensure growth inhibition across the cell population. We also added SYTOX Green given its widespread use in membrane permeabilization assays. To analyze the data, we developed a computational pipeline to extract quantitative information (cell area, intracellular fluorescence intensities, etc.) for each cell over time to assess growth arrest (Figure S2A) and the permeabilization of each cell membrane (see STAR Methods). This is illustrated in Video 1, which shows a representative example of a cell treated with CecA, where permeabilization of both the outer and inner membranes is indicated by the loss of the periplasmic and cytoplasmic fluorescent proteins, respectively.

The tested AMPs fall into two phenotypic classes based on whether cell growth arrest is predominantly associated or not with inner membrane permeabilization to proteins.

To begin, we analyzed the SYTOX Green uptake in cells treated with the different AMPs. To our surprise, the intracellular SYTOX Green signal differed widely across all ten AMPs investigated (Figure 1D), making it difficult to select a consistent threshold for defining IM permeabilization. In contrast, monitoring the loss or change in signal from the fluorescent proteins mScarlet-I and mTagBFP2 gave

a reliable and robust method to monitor the permeabilization of each membrane to proteins over time (see STAR Methods and Video 1 as one example).

Under our experimental conditions, all tested AMPs displayed some IM-permeabilizing activity, albeit to varying degrees (Figure 1E, see STAR Methods for details on IM permeabilization detection). Even the proline-rich peptides PR-39, Bac7, and Tur1A, which are typically regarded as nonmembrane-disruptive at near-MIC concentrations (Boman et al., 1993; Mardirossian et al., 2018; Podda et al., 2006; Scocchi et al., 2011), exhibited some degree of IM permeabilization (Figure 1E). Although their activity was considerably lower than that of other AMPs, Bac7 and especially PR-39 showed higher permeabilization rates than the control antibiotics, rifampicin (Rif) and spectinomycin (Spect), which inhibit transcription and translation, respectively (Figure 1E).

The distinction among AMPs became clearer when we compared the timing of growth arrest and IM permeabilization to the fluorescent protein markers (Figures 1F and S2B). This resulted in two major classes. For class I (CecA, Tac1, Mag2, Mltt, LL-37, HBD-3, and Indo), IM permeabilization to proteins was *predominantly* (i.e., in most cells) associated with the growth arrest (Figure 1F). For some of these peptides, we observed considerable cell-to-cell variability in the timings of IM permeabilization and growth arrest, occurring earlier in some cells and later in others (Figure 1F). However, regardless of this variability, both events remained closely associated in time, as indicated by the data points falling close to the $y = x$ diagonal in the plots (dashed line, Figure 1F), resulting in near-zero residuals from the diagonal (Figure S2B). The observed variability in event timings across cells highlights the importance of using a time-resolved method with single-cell resolution. For class II AMPs (PR-39, Bac7, and Tur1A), when IM permeabilization did occur, it occurred after the growth arrest (Figure 1F), resulting in high residuals (Figure S2B). This observation indicates that IM permeabilization was not the underlying cause of cell growth inhibition for these peptides.

AMPs can be further categorized based on their outer membrane effect.

The class I phenotype (predominant association between growth arrest and IM permeabilization) could be further subdivided into two types based on the relative timing of permeabilization between the two membranes (Figure 2A). For type A, OM permeabilization to proteins predominantly occurred before or near the time of IM permeabilization ($t_{OM\ perm} \leq t_{IM\ perm}$). This phenotype was prevalent for cells exposed to CecA, Tac1, LL-37, or Mag2. It was characterized by the high efficiency and rate of OM

permeabilization among cells that became IM-permeabilized (Figure 2B), along with the strong temporal concurrence between these two permeabilization events (Figure 2C). This is illustrated in Video 1 and its corresponding fluorescence kymographs (Figure 2D) showing how a representative CecA-treated cell abruptly stopped growing and shrunk in size at approximately the same time as the periplasmic mScarlet-I signal disappeared, marking the OM permeabilization event. Almost immediately after, the cytoplasmic mTagBFP2 signal vanished due to IM permeabilization.

For type B, the sequence of events was less intuitive, as the OM was either permeabilized well after the IM or was not permeabilized at all during the course of the experiment ($t_{OM\ perm} > t_{IM\ perm}$, Figure 2A). Video 2 and its corresponding kymographs showcase an example of this type B phenotype for a representative Indo-treated cell. Permeabilization of the inner but not outer membrane was evident by the periplasmic mScarlet-I signal moving into the cytoplasm and mixing with mTagBFP2. As previously demonstrated for growth-arrested cells with protein synthesis inhibitors (Balleza et al., 2018; Bevis & Glick, 2002; Hebisch et al., 2013; Megerle et al., 2008), the signal intensity of the fluorescent proteins in Indo-treated cells increased after growth arrest due to the delayed fluorophore maturation, before subsequently decreasing as a result of photobleaching (Video 2). The transient increase in fluorescent protein signal was exacerbated by the cell shrinkage. For Indo, we did not observe any OM permeabilization event during the experiment (Figure 2B). For HBD-3, OM permeabilization occurred at a low rate in IM-permeabilized cells (Figure 2B) and when it happened, it was substantially after the IM permeabilization event (Figures 2C and S3A).

Quantitatively, treatment with class I type A peptides (CecA, LL-37, Mag2, and Tac1) resulted in an abrupt drop in mScarlet-I and mTagBFP2 signals inside cells due to the permeabilization of both membranes (Figure 2F). Class I type B also caused IM permeabilization, but the cells maintained both fluorescent protein signals during all or part of the experiment (Figures 2E-G and S3A). To track this specific phenotype, the timing of IM permeabilization was determined by calculating the difference of the mScarlet-I signal between the cell periphery (periplasm) and the cell interior (cytoplasm). This metric $\Delta(\text{peri, cyto})_{\text{mScarlet-I}}$ changed rapidly from a positive value to a negative one once mScarlet-I proteins entered the cytoplasm due to IM permeabilization (Figure 2G). Thus, our analysis shows that even though class I type B AMPs predominantly permeabilize the IM of *E. coli*, they are largely not lytic (i.e., they do not release protein content into the environment) at the time of growth arrest.

The late IM permeabilization events occasionally observed with class II PR-39, Bac7, and Tur1A (Figure 1F) were also predominantly non-lytic events. Neither mScarlet-I nor mTagBFP2 signal was lost; instead, IM permeabilization was apparent by the internalization of mScarlet-I into the cytoplasm (Figure S3B-D), indicating that the OM remained intact.

The rate of SYTOX Green uptake by cells is affected by the integrity of both inner and outer membranes.

In light of the results discussed above, we re-analyzed the SYTOX Green data relative to the start of growth inhibition (Figure S2A) instead of relative to the time of AMP addition to normalize for cell-to-cell variability (Figure S4). With this realignment, the dye uptake rate was the lowest for cells treated with PR-39, Bac7, and Tur1A consistent with their class II affiliation. Conversely, the incorporation rate of SYTOX Green was the highest for class I type A AMPs CecA, Tac1, Mag2, and LL-37 (Figure S4). The SYTOX Green uptake for class I type B Indo and HDB-3 was higher than for class II but still considerably lower than for their type A counterparts (Figure S4, see Videos 1 vs 2 for a visual comparison). Only Mltt, which falls between types A and B in terms of phenotypic classification (Figure 2B-C), caused a large STYOX Green uptake (Figure S4). These results indicate that the OM acts as a partial barrier for SYTOX Green and that the OM-breaching activity of class I type A AMPs greatly facilitates dye influx by creating larger or additional holes. Thus, differences in AMP activity against the IM and OM contribute to the large variability in dye uptake observed across AMP treatments.

This analysis further highlights the value of using an approach with both temporal and single-cell resolution. SYTOX Green uptake appeared lower for class I type B Indo compared to class II PR-39 up to 60 min post-treatment (Figure 1D, zoom). However, by aligning the data for each cell relative to its time of growth inhibition, we circumvented the compounding effect from cell-to-cell variability in timings. With this correction, the average SYTOX Green uptake for Indo becomes higher than for PR-39 (Figure S4, zoom), consistent with their differing membrane activities (Figure 1E-F). This correction is not possible for conventional bulk assays where dye incorporation is typically measured at a given time after AMP addition.

Growth inhibition by the class I AMPs is also associated with intracellular rearrangement of ribosomes and DNA.

As mentioned above, various AMPs, including some from our panel, have been reported to bind to intracellular targets (Cardoso et al., 2019; Ghosh et al., 2014; Hsu, 2005; Scocchi et al., 2009, 2011; Subbalakshmi & Sitaram, 1998; Yonezawa et al., 1992) or cause different forms of cytoplasmic phase separation (Boeynaems et al., 2023; Chongsiriwatana et al., 2017; Sneideris et al., 2023; Zhu et al., 2019). Therefore, we next examined whether our set of cationic AMPs caused intracellular effects at the time of growth inhibition. We focused on the chromosome (which folds into a structure known as the nucleoid) and the ribosomes because these two large anionic cytoplasmic components are often proposed as intracellular targets of AMPs (Cardoso et al., 2019; Le et al., 2017), and the AMP LL-37 has been shown to perturb their intracellular organization (Zhu et al., 2019). During unperturbed growth, most ribosomes are bound to mRNAs and are engaged in translation, forming monosomes and polysomes (collectively referred to as polysomes for simplicity). Because of their large size relative to the DNA mesh (Xiang et al., 2021), polysomes are largely excluded from the nucleoid, resulting in ribosomal accumulation in DNA-depleted regions (Bakshi et al., 2012; Gray et al., 2019; Lewis et al., 2000; Linnik et al., 2024; Sanamrad et al., 2014; Xiang et al., 2021). This segregation pattern can be visualized by microscopy using well-characterized fluorescent protein fusions to ribosomal and DNA-binding proteins such as RplA-GFP and HupA-mCherry, respectively (Papagiannakis et al., 2024; Xiang et al., 2021). Their anticorrelation in localization results in negative signal correlation factor (SCF) values (Gray et al., 2019).

To visualize several intracellular components at the same time, we used a strain (CJW7753) that expresses three different markers (Figure 3A): RplA-GFP, HupA-mCherry, and mTagBFP2. Time-lapse imaging under the same standardized conditions as above demonstrated that the intracellular distribution of ribosomes and DNA changed abruptly when cells were exposed to class I type A AMPs. This is illustrated with CecA where the ribosome (RplA-GFP) and DNA (HupA-mCherry) signals transiently mixed near the time of growth arrest (Video 3 and Figure 3B). This sudden mixing was followed within a few minutes by re-separation (unmixing) of the ribosome and DNA signals (Figure 3B), as quantified by a transient peak in positive SCF values in individual cell trajectories (Video 3). When all cell trajectories were aligned by the SCF peak, we observed a clear temporal pattern across CecA-treated cells (Figure 3C). The SCF peak (i.e., peak of ribosome/DNA mixing) occurred near the time of growth arrest, coinciding with or slightly preceding the time of mTagBFP2 signal loss,

indicating IM permeabilization (Figure 3B and C). Re-segregation of the ribosome and DNA signals occurred concomitantly with DNA compaction (Video 3 and Figure 3C), which was quantified by a reduction of the nucleocytoplasmic (NC) ratio (DNA signal length divided by the cell length). We found that the mixing of ribosome and DNA signals (SCF peak), which is known to be associated with polysome depletion and hence protein synthesis inhibition (Bakshi et al., 2012; Gray et al., 2019; Lewis et al., 2000; Linnik et al., 2024; Xiang et al., 2021), closely correlated in time with the loss of mTagBFP2 signal (i.e., membrane permeabilization), often slightly preceding it (n = 314 cells, Figure 3B and C).

We found that the same abrupt and transient mixing of ribosome and DNA signals (SCF peak) occurred near the time of growth arrest for the six other class I AMPs (Figure 3D), as indicated by the data points lying close to the $y = x$ diagonal. At later timepoints, the behavior of the ribosome and DNA signal was more variable. We did not carefully characterize these late events as the focus was on the events that occur near the time of growth inhibition.

Similar intracellular rearrangements occur with class II AMPs but with slower kinetics.

Remarkably, despite their difference in membrane activity, class II AMPs PR-39, Bac7, and Tur1A induced a mixing between ribosome (RplA-GFP) and DNA (HupA-mCherry) signals similar to class I AMP CecA, resulting in positive SCF values (Figure 4A and Video 4 for a PR-39-treated cell example). This mixing was followed by both ribosome/DNA re-segregation (decreasing SCF values) and DNA compaction (decreasing NC ratio). However, the kinetics of these events were considerably more gradual for these class II peptides, as shown by the broader average SCF peaks and slower decays in NC ratio for both PR-39, Bac7, and Tur1A (Figures 4B and S5A-B) compared to class I CecA (Figure 3B). For all three class II AMPs, the timing of the ribosome/DNA mixing (SCF peak) coincided with the onset of growth inhibition (Figure 4C). Thus, all ten AMPs tested caused the same DNA/ribosome mixing event near the time of growth inhibition but with different kinetics depending on their designated class.

Higher peptide concentrations can decrease cell-to-cell variability and increase the average speed of antibacterial action.

We were surprised by the cell-to-cell variability in the timing of growth arrest (and correlated events) for some peptides (Figure 1F) and wondered whether increasing or decreasing the peptide concentration relative to its MIC may alter this variability. To examine this possibility, we selected three class I peptides, CecA, LL-37, and Mltt, which exhibit a low, intermediate, and high cell-to-cell variability in growth arrest timing at a concentration corresponding to 2X MIC (Figure 1F). We also tested two class II peptides (Bac7 and PR-39) for comparison. If the peptide concentration mattered, we expected to see a higher cell-to-cell variability at 1X MIC and a lower one at 10X MIC. This is indeed the trend that we observed (Figure S6). In addition, higher concentrations considerably reduced the delay between peptide addition and growth arrest. This was particularly true for the examined class I AMPs, which became very fast-acting at concentrations that exceeded their MICs compared to the class II peptides (Figure S6).

Intracellular absorption differs among fluorescent AMP derivatives.

LL-37 tagged with a fluorophore has been shown to accumulate at high levels inside cells (Snoussi et al., 2018; Zhu et al., 2019). Since LL-37 is a class I AMP, membrane permeabilization may contribute to this rapid peptide uptake. If so, then there could be a considerable difference in the rate of peptide absorption between class I and class II peptides. To test this possibility, we commissioned the synthesis of fluorescent 5-TAMRA conjugates to AMPs with high membrane-permeabilizing activity: class I type A peptides CecA, Tac1, and LL-37 (Figure 1E-F). For comparison with peptides with lower membrane-permeabilizing activity, we also obtained 5-TAMRA conjugates to class II PR-39 and Bac7 (as well as a synthetic peptide, DJK-5, which is discussed in a section below). We found that these fluorescent AMP derivatives retained antibacterial activities, featuring slightly higher or lower MIC values than the unconjugated peptides (Figure S1D). To minimize potential secondary effects associated with the fluorophore tag, we treated cells with unlabeled AMPs at 2X MIC, spiked with the same concentration (50 nM) of fluorescently labeled derivatives.

For all three class I peptides CecA, Tac1, and LL-37 (spiked with their 5-TAMRA-tagged version), we observed rapid uptake and massive intracellular accumulation of fluorescence signal within just 10 min of growth inhibition (Figure 5A). This stood in striking contrast to class II PR-39 and Bac7

derivatives (Figure 5A). At that 10-min timepoint, the intracellular signal from 5-TAMRA conjugated to CecA, Tac1, and LL-37 was ~400-1000 times higher than for the PR-39 or Bac7 conjugates (Figure S7A). This discrepancy is consistent with the large difference in SYTOX Green uptake and intracellular accumulation between AMP classes (Figure S4), likely due to their differences in membrane permeabilization activity (Figure 1E-F).

The accumulation of AMPs inside cells implies that they bind to intracellular targets. Interestingly, when we examined the fluorescently labeled AMP signal at late time points of treatment—when the ribosome (RplA-GFP) and the DNA (HupA-mCherry) signals are well separated through mutual exclusion—it was not homogeneously distributed inside cells. Instead, 5-TAMRA-tagged Tac1, CecA, and LL-37 were found to co-localize with the ribosome signal in RplA-msfGFP-expressing cells and to anti-correlate with the DNA signal in HupA-msfGFP-expressing cells (Figures 5B and S7B-C). Colocalization with ribosomes, along with DNAexclusion, was also apparent for the commercially available TRITC-labeled LL-37 (Figure S7D). At the population level, the correlation between each AMP signal and the ribosome marker (RplA-msfGFP), as well as the anti-correlation with the DNA marker (HupA-msfGFP), were quantitatively confirmed by the corresponding positive and negative correlation values, respectively (Figure 5C).

This localization pattern was also observed for 5-TAMRA-PR-39 and 5-TAMRA-Bac7, spiked at 25:75 and 50:50 labeled-to-unlabeled ratios, respectively, to enhance their fluorescent signal (Figure 5C). However, the signal correlation values were less convincing due to limited intracellular peptide absorption. Notably, in a minority of cells treated with 5-TAMRA-PR-39, strong intracellular signal was detected, presumably due to a late IM permeabilization event that promoted the peptide entry, similar to class I AMPs. In these cells, the colocalization of 5-TAMRA-PR-39 with ribosomes (RplA-msfGFP) and its exclusion from the DNA (HupA-msfGFP) were readily apparent (Figure 5D).

The fact that all examined fluorescent AMP derivatives are excluded from the DNA region and colocalize with ribosomes to varying degrees suggests that ribosomes may be major intracellular targets and that their high abundance might contribute to the large cellular absorption of AMPs upon membrane permeabilization. The colocalization of ribosomes with fluorescent AMPs does not rule out other intracellular targets. It is, however, worth noting that most proteins in bacteria have a net negative charge and that when the net charge of GFP is changed from -7 to +25, this cationic version binds to and colocalizes with ribosomes in the *E. coli* cytoplasm (Schavemaker et al., 2017). This

suggests that the observed colocalization between ribosomes and cationic AMPs is likely driven by electrostatic interactions.

Class II AMPs are more effective than class I peptides against high bacterial cell densities.

Membrane-permeabilizing activity is widely regarded as a desirable characteristic in an AMP. Indeed, class I AMPs exhibit faster antibacterial activity kinetics compared to class II AMPs (Figure 3B-C vs Figure 4A-B), particularly at high concentrations (Figure S6). However, the uptake kinetics of fluorescent derivatives suggest that membrane permeabilization, which is predominant with class I peptides, promotes high intracellular absorption (Figure 5A). High accumulation of LL-37 has been shown to cause a phenomenon known as the inoculum effect (Snoussi et al., 2018) where higher concentrations of an antibacterial agent are needed for increasing population (or inoculum) size.

These contrasting kinetics between class I and II AMPs inspired us to think about potential trade-offs and how they may be relevant under physiological contexts. In our experiments described above, *E. coli* cells were present at a low density and the AMPs were delivered homogeneously. Inside a host, the delivery of AMPs can be polarized, for example, when they are secreted by the mammalian intestinal epithelium into the mucus in the gut lumen (Figure 6A). In vivo, immune cells such as neutrophils may encounter dense cell populations (Figure 6A), for example, when the infection has reached a high level of bacterial load or when the pathogen assembles into biofilms, which often contributes to chronic infections (Costerton et al., 1999; Kostakioti et al., 2013). To mimic both effects (polarized delivery and high cell density), we built a microfluidic device modeled on an earlier design (Lambert & Kussell, 2014). This device contains wide trenches where bacterial cells can grow at a high cell density under a constant flow of fresh nutrients that rapidly diffuse from the “feeding” channel into the trenches (Figure 6B). Excess cells at the top of the trenches are continuously removed by the flow. AMPs are supplemented in the growth medium, creating a constant concentration in the feeding channel. Due to diffusion, their delivery in the cell-filled trenches is polarized, with cells at the top of the trenches encountering the peptides first. We predicted that, in this context, the class I AMPs, unlike class II peptides, would be rapidly absorbed by the first cells they permeabilize, thereby promoting their own cytoplasmic entry. This self-promoted uptake would reduce their availability, making them less effective at inhibiting growth across the entire population compared to class II AMPs.

Our findings support this prediction. Once reaching the trenches, class I type A AMPs CecA, LL-37, Tac1, and Mag2 at 2X MIC concentrations effective at inhibiting growth at low cell densities (Figures 1-5) only affected cells near the top of the trenches (Videos 5-8). These cells stopped growing and became brighter in signal due to DNA compaction and fluorophore maturation of the fluorescent ribosome and DNA markers (illustrated with a snapshot for LL-37 in Figure 6C and shown in timelapse sequences for all four class I type A peptides in Videos 5-8). The neutralized cells shielded the cells below, presumably by rapidly absorbing the incoming peptides. As a result, the protected cells continued to grow, occasionally pushing the dead cells out of the trenches. This is consistent with the heterogeneous killing behavior of LL-37 observed in dense populations (Snoussi et al., 2018). Class I type A/B Mltt had a similar effect (Video 9). The class I type B Indo, which disrupts the IM but not the OM (Figure 2B, E, and G), performed slightly better by inhibiting the growth of cells located further into the trenches (Figure 6C and Video 10). However, Indo still failed to stop the growth of most cells in the trenches at concentrations that were effective against low cell densities (Figures 1-2). In striking contrast, class II AMPs PR-39, Bac7, and Tur1A were able to inhibit cell growth throughout the entire wide trenches (Figure 6C and Videos 11-13). We concluded that the slow uptake of class II peptides allows them to diffuse throughout the trench, resulting in growth inhibition of the entire cell population.

We discovered that LL-37 exhibits a low level of fluorescence (predominantly in the red channel) at 30°C for reasons that are currently unclear and under investigation. We exploited this property to visualize the diffusion of the peptide and its cellular absorption at concentrations as high as 20 μM, which corresponds to 20 times the MIC needed to neutralize cells at low density. We predicted that higher concentrations would increase antibacterial activity across the trenches. In empty trenches, the fluorescence of LL-37 (20 μM, 20X MIC) rapidly spread across the entire length of the trenches (Video 14), indicating that diffusion itself was not limiting. In contrast, LL-37 was unable to diffuse across nearby trenches containing cells. Instead, it was rapidly absorbed by the frontline cells where it accumulated at a high level, as evidenced by the bright LL-37 fluorescence signal (Figure 6D and Video 14). The higher concentration of LL-37 helped increase the depth of cell growth inhibition along the trenches. However, even at a concentration (20 μM) equivalent to 20X MIC, only the top cell section of the trenches was neutralized, forming a protective crust (Figure 6D). This crust resulted in the compression of the growing cells below, with their growth ultimately pushing the protective crust of dead cells out of the trenches (Figure 6D and Video 14).

We did not test concentrations higher than 20X MIC (20 μM), as such high doses become toxic for eukaryotic cells (Johansson et al., 1998; Oren et al., 1999). Altogether, our results indicate that membrane permeabilization carries a trade-off, which has immunological implications (see Discussion).

The same phenotyping principles apply to synthetic mimics TM1 and DJK-5.

Given the prospect of AMPs as antimicrobial therapeutics, significant efforts have been invested in developing synthetic AMP mimics that retain the potency of natural peptides while addressing their limitations (e.g., bioavailability, toxicity, and production costs) (Svenson et al., 2022). These mimics are often smaller and more resistant to protease cleavage due to the incorporation of non-natural chemical modifications. To examine whether our phenotype-based classification framework is broadly generalizable, we selected two synthetic AMP mimics with different chemistries, sequences, and characteristics.

The first one was TM1, which is a 12-mer peptoid (H-(*N*Lys-*N*spe-*N*spe)$_4$-NH$_2$, where *N*Lys is *N*-(4-aminobutyl)glycine and *N*spe is *N*-S-(1-phenylethyl)glycine) with broad-spectrum antibacterial activity (Chongsiriwatana et al., 2008, 2017). Peptoids are protease-resistant because they differ from peptides by having the side chains attached to the backbone amide nitrogen instead of the α-carbon (Zuckermann et al., 1992). We found that at 5 μM (2X MIC, Figure S1A), TM1 behaves as a class I type B AMP. At low cell density, growth arrest was associated with cell shrinkage (decrease in cell length) and the internalization of periplasmic mScarlet-I (Figures 7A and S8A). IM permeabilization occurred across almost all (82 out of 84) analyzed cells at a high rate (Figure 7B), coinciding with the growth arrest (Figures 7C and S2B). OM permeabilization was infrequent (15 cells out of 82) and typically delayed relative to IM permeabilization (Figures 7D and S8B). At this same concentration, TM1 only inhibited a fraction of the cells in the dense populations of wide trenches (Figure 7E and Video 15). Similar phenotypes were observed for the class I type B Indo (Figures 2E, 2G, and 6C, and Video 10).

Our second synthetic AMP mimic, the 12-mer D-enantiomeric peptide DJK-5 (Figure 1A), was selected because of its known efficacy against biofilms (De La Fuente-Núñez et al., 2014, 2015). In light of our results with dense populations in the wide trenches (Figure 6), we hypothesized that DJK-5 may share properties with class II AMPs that allow it to be effective against the high bacterial

densities found in biofilms. Consistent with this speculation, we found that DJK-5 predominantly displayed class II peptide behavior. While DJK-5 resulted in IM permeabilization (mScarlet-I internalization) in many (72%) cells (Figure 7B), this event was usually delayed relative to the growth arrest. This is illustrated at the single-cell level (Figure 7F and S8C) and quantified at the population level (Figures 7G and S2B). Combined, approximately 90% (169 out of 187) of DJK-5-treated cells either did not experience IM permeabilization during the 230-minute experiment or did so only after a delay of 10 min or more post-growth arrest.

Permeabilization of the OM (loss of both mScarlet-I and mTagBFP2) was also observed in a fraction of DJK-5-treated cells (~40%, Figure 7D) but typically after that of the IM (as illustrated in Figures 7F and S8C-D). As a result of these combined properties, the average cell absorption rate and accumulation of fluorescent 5-TAMRA-DJK-5 were similar to the fluorescent derivative of class II PR-39 and Bac7 when examined under the same conditions (Figure 5A and S7A).

Consistent with a class II behavior, DJK-5 demonstrated efficacy against high cell densities by fully inhibiting cell growth in wide trenches (Video 16 and Figure 7H). These results suggest that the critical factor for efficacy against dense cell populations is not the absence of membrane permeabilization, as it can indeed occur for DJK-5, PR-39, Bac7, and Tur1A (Figures 1E-F, S3B-D, 7B, 7G, and S8B). Rather, the key appears to lie in the timing: a sufficient delay between growth inhibition and inner membrane permeabilization is required for efficient neutralization of high bacterial densities. This delay provides enough time for the peptides to diffuse across a dense cell population before starting to permeabilize their membranes. Without this time interval, the peptides would be prematurely sequestered into the cytoplasm of the first encountered cells, limiting their further diffusion and reducing their overall effectiveness.

DISCUSSION

In this study, we describe a time-resolved single-cell phenotyping method to study and classify AMPs and peptidomimetics. Temporal resolution is critical for classifying this family of antibacterial agents, as diverse AMPs and mimics can cause the same cellular effects at different times relative to growth inhibition (Figures 1-5 and 7). Single-cell resolution is equally important given the cell-to-cell variability in timing and the importance of probing the intracellular redistribution of molecules (e.g., mScarlet-I internalization) during AMP treatment (Figures 1-4 and 7).

Remarkably, all examined AMPs, regardless of their class designation, adhere to a set of common principles. They elicit shared intracellular effects, including a ribosome/DNA mixing concurrent with growth inhibition. Mechanistic studies suggest that such a ribosome/DNA mixing event corresponds to polysome loss and protein synthesis inhibition (Bakshi et al., 2012; Gray et al., 2019; Lewis et al., 2000; Linnik et al., 2024; Xiang et al., 2021). Another common feature between the two classes is that their fluorescent derivatives preferentially colocalize with ribosomes and not the DNA (Figures 5B-D and S7B-E). The phenotypic convergence across all the examined peptides is remarkable given their diversity in sequence, structure, and characteristics (Figure 1A-B and Table S1), suggesting that a shared physicochemical property (e.g., high positive charge density) likely governs these actions.

The distinction between the two classes of peptides appears to lie in their kinetics, which are marked by a difference in membrane-permeabilizing activity. Importantly, the distinction cannot be simply reduced to one class being capable of permeabilizing membranes and the other not. While the frequency of IM permeabilization is generally high with class I AMPs (Figure 1E), it is not negligible with class II peptides. Under our experimental conditions, the IM became permeabilized in the majority (> 60%) of cells treated with PR-39 or DJK-5 (Figures 1E and 7B). The key distinction is the timing. For class I, IM permeabilization occurs nearly simultaneously with the cell growth arrest (Figures 1F, 7C, and S2B), while for class II, it is generally delayed relative to growth inhibition (Figures 1F, 7G, and S2B).

Our findings suggest that these differences between classes lead to major trade-offs in antibacterial activities. Through membrane permeabilization, class I peptides self-promote their intracellular uptake by effectively creating their own entryways, whereas class II AMPs such as PR-39, Bac7, and Tur1A have been shown to use (at least in part) cellular transporters to facilitate their passage through the cell envelope (Mardirossian et al., 2018; Mattiuzzo et al., 2007). Mutations that disrupt the activity of this transporter result in reduced susceptibility (Mardirossian et al., 2018; Mattiuzzo et al., 2007; Pränting et al., 2008), suggesting that class II peptides may be more prone to resistance. On the other hand, the high membrane-permeabilizing activity of class I AMPs comes at the cost of their high cell absorption. Consequently, class I AMPs perform poorly against large cell densities because they are rapidly sequestered by the first encountered cells, which act as shields for those behind them. Conversely, the cell absorption of class II peptides is low because membrane permeabilization does not happen or it is delayed relative to growth inhibition, allowing these peptides to diffuse further while still inhibiting cell growth. As a result, class II peptides are more

effective against large cell densities. These trade-offs may represent distinct immune defense strategies adapted to different infection challenges, as both peptide classes can be produced by the same organism (e.g., bovine AMPs Indo and Bac7). For example, a fast-acting class I peptide may be advantageous to quickly neutralize an early infection when the bacterial burden is low, especially if the bacterial offender is motile and can quickly move away from the site of AMP release. In contrast, the low-absorption properties of a class II AMP likely confer an advantage over a class I if the infection has reached a high cell density. One class may be more potent than the other depending on the scale or type of infection.

These trade-offs may also be relevant to biofilms. Biofilm resilience, which contributes to recurring antibiotic-resistant infections (Costerton et al., 1999), has been linked to the expression of biofilm-specific genetic pathways and the presence of a protective extracellular matrix (Kostakioti et al., 2013). The shared properties between class II AMPs and anti-biofilm DJK-5 (Figures 1F, 5A, 6C, and 7F-H) suggest that the high cell density in biofilms may also contribute to their resilience, particularly against class I AMPs. High permeabilizing activity against bacterial membranes is often considered an attractive property for synthetic AMP mimics as therapeutic agents. In the specific context of biofilms, our results indicate that a low or delayed membrane-permeabilizing activity (as with class II peptides) may be preferable.

Regarding membrane permeabilization, terms such as lytic and membrane-permeabilizing are often used interchangeably in the AMP literature. However, Gram-negative bacteria possess two membranes, the OM and the IM, which have distinct compositions. By using cytoplasmic and periplasmic fluorescent proteins with distinct spectral properties, our method demonstrates that differences in permeabilization susceptibility between the two membranes subdivide class I AMPs into two types (Figure 2). Type A peptides permeabilize both membranes near the same time (Figure 2C-D and F), resulting in the highest rate of SYTOX Green (Figure S4). Comparatively, dye uptake is considerably slower for type B (Figure S4), which permeabilizes only the IM, keeping both periplasmic and cytoplasmic protein markers within the boundaries of the intact OM (Figure 2E, G, S3A, 7A, and S8A). Thus, class I type B peptides are IM-permeabilizing but not lytic, at least not at the time of growth arrest. This distinction among class I defense peptides likely has immunological implications as the antibacterial activity of type A results in an immediate release of intracellular protein antigens, whereas type B does not.

Our classification framework is currently based on using *E. coli* as a bacterial target. Moving forward, it will be interesting to implement our approach on other bacteria, including Gram-positive bacteria, multidrug-resistant pathogens, and AMP-resistant strains. This will help refine the classification and expand our understanding of resistance mechanisms. Another exciting prospect will be to scale up the phenotype profiling to a large number of AMPs and synthetic variants. Our study highlights a few interesting sequence features in peptides with regard to their classification (Figure 1). For example, the inclusion of proline-devoid DJK-5 in the same class II as the proline-rich PR-39, Bac7, and Tur1A suggests that their shared sequence features—the presence of arginines and the absence of lysines— may be more critical for class II behavior than the abundance of prolines. While our set of selected peptides is too small to draw conclusive relationships between sequence and function, a large-scale study integrated with machine learning models (Liu et al., 2025; Wan et al., 2024) holds the potential to bridge the gap between the sequence and function of antimicrobial peptides. Bridging this gap is essential to achieve predictive power and unlock their promise as next-generation therapeutics.

STAR METHODS

Strains and growth conditions

For all experiments and *E. coli* strains, cells were grown in a medium (M9gluCAAT) with M9 salts (33.7 mM Na_2HPO_4, 22mM KH_2PO_4, 8.55 mM NaCl, 9.35 mM NH_4Cl), 0.2% (w/v) glucose, 0.4% (w/v) casamino acids, 1 mM $MgSO_4$, 0.3 mM $CaCl_2$, 1 μg/mL thiamine, and trace elements (13.4 mM ethylene-diamine-tetra-acetic-acid (EDTA), 3.1 mM $FeCl_3$-$6H_2O$, 0.62 mM $ZnCl_2$, 76 μM $CuCl_2$-$2H_2O$, 42 μM $CoCl_2$-$2H_2O$, 162 μM H_3BO_3, 8.1 μM $MnCl_2$-$4H_2O$). Prior to every experiment, cells were first inoculated into M9gluCAAT and grown to stationary phase at 37°C (unless indicated otherwise). To obtain steady-state exponentially growing cells prior to the experiment, the culture was then re-diluted by 1/10,000 or more in fresh medium and grown at 37°C until it reached an optical density at 600 nm (OD) of 0.2-0.4.

All the strains used in this study were derived from MG1655 (ATCC 47076), which was used to estimate the minimum inhibitory concentration (MIC) for all the studied peptides (or peptoids) using a microplate reader (Figure 1A). To detect the timing of outer and inner membrane permeabilization

to proteins, we constructed the strain CJW7845, which carries two freely diffusing fluorescent proteins: mScarlet-I in the periplasm and mTagBFP2 in the cytoplasm.

Construction of CJW7845 was done by transforming pBAD-mTagBFP2 plasmid (Addgene #34632, a gift from Vladislav Verkhusha; (Subach et al., 2011)) into an *E. coli* strain expressing a periplasmic mScarlet-I reporter (Cañas-Duarte & J, 2021), as previously described (Chung et al., 1989). Transformants were restreaked once on fresh selection plates and confirmed via microscopy.

To monitor the intracellular perturbations of ribosomes and DNA over time while assessing the cell envelope integrity, a strain (CJW7753) carrying a chromosomally expressed HupA-mCherry and RplA-GFP, as well as a plasmid-expressed cytoplasmic mTagBFP2 was used (Papagiannakis et al., 2024).

For both strains CJW7845 and CJW7753, mTagBFP2 expression was induced by supplementing the medium with 0.2% (w/v) arabinose. Ampicillin (100 μg/mL) was added to the growth medium of the liquid culture to maintain the plasmid-expressing mTagBFP2 but was not present in the microwell medium during the imaging experiment.

To probe the spatial localization of ribosomes and DNA with respect to fluorescently labeled AMPs, we used strains CJW7020 (Gray et al., 2019) and CJW7859 expressing RplA-msfGFP and HupA-msfGFP, respectively).

Strain CJW7859 was constructed as follows. The monomeric superfolder GFP (msfGFP) coding sequence together with a kanamycin resistance cassette flanked with flippase recognition target (FRT) sites were amplified from a pKD13 vector (Datsenko & Wanner, 2000) encoding msfGFP without its start codon, preceded with a sequence encoding a glycine/serine-rich linker (GSGSGS) (strain CJW6871 (Gray et al., 2019)), using primers 5'-GGCATTTGTTTCTGGCAAGGCACTGAAAGACGCAGTTAAGGGCAGCGGCAGCGGCAGCTC-3' and 5'-AAACCACCCCTTCGTTAAAACTGTTCACTGCCACGCAATCATCCGTCGACCTGCAGTTCG-3'.
Polymerase chain reaction (PCR) was performed to add homologous sequences to the 3-end region encoding the HupA C-terminus and the downstream region and to remove the *hupA* stop codon, yielding an encoded C-terminal HupA-msfGFP fusion. The amplified product was transformed by electroporation into MG1655 containing pSim6. The plasmid expresses the Red recombineering proteins (encoded by *exo*, *bet*, and *gam*) under the control of the native λ phage pL promoter and temperature-sensitive cI857 repressor, whose expression can be induced by heat-shock as previously described (Sharan et al., 2009). The pSim6 plasmid was kindly provided by the National

Cancer Institute. Briefly, cells were grown at 30°C to mid-exponential phase and the synthesis of the recombineering proteins was induced for 15 min at 42°C prior to making cells electrocompetent. Mutants were selected on kanamycin, and the correct integration was verified by PCR and sequencing of the modified genomic region using primers 5'-TGTCGTACCTGGAGTCTTCC-3' and 5'-TTCAGCAAATCCACTGGCGG-3'. The modification was moved to a clean wild-MG1655 strain in which no recombineering system was expressed via P1 transduction as previously described (Thomason et al., 2007). Transductants were confirmed via PCR and sequencing of the modified region using the same primers as above. A single colony was grown and transformed with temperature-sensitive pCP20, expressing the site specific Flp recombinase to excise the kanamycin cassette used for initial selection, as previously described (Cherepanov & Wackernagel, 1995). Briefly, transformants were selected on LB plates containing chloramphenicol (30 µg/mL) at 30°C and streaked on LB plates at 42°C overnight to induce Flp recombinase expression and loss of pCP20 plasmid. The loss of FRT-flanked kanamycin resistance cassette was confirmed by PCR and the lack of growth in the presence of kanamycin (50 µg/mL). The loss of pCP20 was confirmed by the lack of chloramphenicol resistance.

Sources and preparation of antimicrobial peptides/peptoid

Lyophilized powders of LL-37 (AS-61302), human β-defensin 3 (AS-60741), magainin 2 (AS-20639), cecropin A (AS-24009), and indolicidin (AS-60999) were purchased from AnaSpec Inc. (California, USA). PR-39 (350590) was purchased from Abbiotec (California, USA). Tachyplesin I (4030734) was purchased from Bachem AG (Switzerland). Bac7 (318782), Tur1A (318733), and DJK-5 (318921) were purchased from NovoPro Bioscience Inc. (Shanghai, China). 5-TAMRA-labeled cecropin A, tachyplesin I, LL-37, PR-39, Bac7, and DJK-5, were commissioned to NovoPro Bioscience Inc. (Shanghai, China) for custom peptide design. TRITC-LL-37 (000-000-M33) was purchased from Rockland Immunochemicals, Inc. (Pennsylvania, USA). For all fluorescently labeled peptides, the fluorescent label was conjugated to the N-terminus. Peptide powders were resuspended in Milli-Q water to stock concentrations of 1 mM (or 0.5 mM for human β-defensin 3), aliquoted, and stored at -20°C. TM1 peptoid (first described as Peptoid 1) was synthesized on an automated peptide synthesizer and purified by reversed-phase high-performance liquid chromatography, as previously described (Chongsiriwatana et al., 2008, 2017). Prior to each experiment, aliquots were diluted in fresh medium to the desired concentration.

Protein sequence analysis and feature extraction

Amino acid sequences of the selected peptides (shown in Figure 1A) were analyzed using custom-written functions in Python to extract physicochemical properties (protein_analysis.py). The GRAVY index was computed using the Kyte-Dolittle scale of amino acids hydropathy values (Kyte & Doolittle, 1982). Polar and hydrophobic fractions were calculated based on the following classification: serine, glutamine, asparagine, glycine, threonine, proline, tyrosine, lysine, arginine, histidine, aspartic acid, and glutamic acid were considered polar amino acids whereas alanine, isoleucine, leucine, methionine, phenylalanine, tryptophan, cysteine, and valine were considered hydrophobic. Net charge calculation included contributions from lysine, arginine, and C-terminal amidation (when present). Molecular weight was computed starting from the sum of the molecular weights of the *n* single amino acids, subtracting *n-1* water molecule's weights (18.015 g/mol) as a result of peptide bond formation, weight loss due to C-terminal amidation (0.98 g/mol, when present), and weight loss due to disulfide bridge formation (2.02 g/mol per cysteine pair).

Determination of minimal inhibitory concentrations and maximum growth rates

To determine the minimal inhibitory concentration (MIC) of the selected AMPs against the parent MG1655 *E. coli* strain, exponentially growing cells were diluted in fresh medium to an OD = 10^{-6} (~500 cells/mL) and mixed 50:50 with titrated AMP concentrations (which were chosen to be over a range that included the MIC) in a 96-well plate (flat bottom with low evaporation lid, 3595, Corning, Arizona, USA). A final OD of 5×10^{-7} corresponds to ~250 cells/mL. OD curves were sampled every 5 min for a total of 48 h using a microplate reader (BioTek Synergy 2, Agilent Technologies Inc., California, USA). Raw data were exported as a text file and analyzed using a custom-written Python script (microplate_reader_analysis.py). To measure maximum growth rates, the log(OD) was fitted using a linear regression over a 12-point moving window (60 min), which provides the instantaneous growth rate (log(OD)/h), from which the global maximum was computed and plotted in Figure S1A and D. The MIC was defined as the minimum AMP concentration for which the maximum growth rate was < 0.2 log(OD)/h within the first 20 h of incubation.

Fabrication of a multiwell microfluidic device for single-cell analysis

The multiwell microfluidic device schematically shown in Figure S1B was built as follows. A solution of 9:1 polydimethylsiloxane (PDMS) and curing agent was first mixed and degassed to remove air bubbles. A silicon rubber O-ring (25.8 mm inner diameter, 3.1 mm in thickness) was glued onto a glass bottom dish (40 mm diameter, 14026-20, from Ted Pella Inc., California, USA). PDMS solution (1 gr) was poured onto the glass dish within the O-ring to form a ~1 mm thin PDMS layer, and cured for > 3 h at 64.5°C. An 8 mm biopsy punch was used to perforate the PDMS thin layer and carve out four independent ~70-μL wells (Figure S1B). The four wells were thoroughly rinsed using 70% (v/v) ethanol and 100% isopropanol and blow-dried using purified air. Cells were immobilized using a protocol for atomic force microscopy (Benn et al., 2019) with some modifications. Briefly, the glass surfaces were rendered hydrophilic using air plasma treatment (45 s at 60 W). Then, a Cell-Tak™ (354240, Corning®, Arizona, USA) solution was prepared by mixing 250 μL of 0.1 M sodium bicarbonate, pH 8.0, 10 μL Cell-Tak™, and 5 μL 1M NaOH (enough to functionalize four wells). This solution (50 μL) was applied to each well for 5 min, rinsed three times with Milli-Q water and blow-dried with purified air. Five microliters of exponentially growing cells (diluted to OD_{600} ~ 0.15) were then spotted into the center of each well for 5 min to allow for cells to be immobilized on the surface. The small 5-μL volume allowed us to immobilize cells only within a small region of the well, thus minimizing cell density effects that may affect the MIC. The wells were then washed three times with fresh medium to remove the cells that did not attach to the surface, after which each well was filled with growth medium (70-80 μL). To minimize water evaporation from the wells during the experiments, ~1 mL of medium was added to the region surrounding the O-ring, which aided in maintaining a high local humidity in proximity of the wells. Experiments were carried out with the lid on.

Fabrication of wide-trench microfluidic device

The design of the wide-trench microfluidics was adapted from the one reported by (Lambert & Kussell, 2014). As reported before (Lin & Jacobs-Wagner, 2022), the master mold was manufactured in the clean room of the School of Engineering and Applied Science at Yale University. UV photolithography (EVG 620 Mask Aligner) was applied on Si wafers with SU-8 photoresist to generate two layers of positive patterns. The lower layer contained the bacterial culture chambers (wide

trenches) while the upper layer contained the large trench for the flowing culture medium. The large feeding region features a ~200 μm width and ~30 μm height. The wide trenches have a width of 7 μm, a depth of ~34-38 μm, and a height of 1.29 μm.

Wide-trench microfluidics chip preparation and experiment

A solution of 9:1 polydimethylsiloxane (PDMS) and curing agent was mixed, degassed to remove air bubbles, poured onto the silicon wafer, and cured at 64.5°C for > 3 h. Once hardened, PDMS chips were cut out from the wafer, and a 1.2 mm biopsy punch was used to create inlet and outlet holes. The current chip design features two independent channels per chip. To allow for a higher temperature during PDMS-glass bonding, the glass bottom part of the dish was used during the following steps (without the plastic support glued to it). Both glass slide and PDMS surfaces were subsequently rinsed with 70% (v/v) ethanol and isopropanol to remove dust and debris and blow-dried with purified air. The glass slide was then placed on a 95°C hot plate for further drying for ~2-3 min. Subsequently, the PDMS chip and glass slide were plasma-treated (for 20 s at 60 W), immediately bonded, placed on a 95°C hot plate for 5 min, and baked at 75°C for ~2 h. The bonded chip was then left to equilibrate at room temperature, and a solution of M9gluCAAT supplemented by 0.08 % Pluronic® F-108 was perfused through the channels, which served to wet the dry PDMS and glass surfaces and to render them more hydrophilic by passivating with Pluronic (which has amphiphilic properties). Pluronic (0.08%) was also supplemented into the growth medium to improve the hydrophilicity of the cell outer membranes, with the intent to reduce cell aggregates. Exponentially growing cells (3 mL) were spun at 6500 rpm for 5 min, resuspended in 50-100 μL (to increase cell density), and loaded into the channels. The cells-loaded chip was then spun at 500 g for 3 min using a three-dimensional-printed holder (design gifted by Dr. Johan Paulsson) to facilitate entry of the cells into the trenches. Before every experiment, all the tubings were sterilized and cleaned by flowing 20% (v/v) bleach, 20% (v/v) ethanol, Milli-Q, and then perfused with 0.08% Pluronic-supplemented medium. Experiments were carried out at 37°C unless indicated otherwise. Flow was achieved by a peristaltic pump (T60-S2&WX10-14-H, Langer Instrument, USA), which was set to deliver a constant flow rate of ~35 μL/min, which was maintained for the whole duration of the experiment, including the AMP treatment.

Microscopy

Images were acquired using a Nikon Ti2-E inverted microscope equipped with a Photometrics Prime BSI back-illuminated sCMOS camera (2048x2048 pixels, 6.5 μm pixel size), a 100X Plan Apo 1.45NA Ph3 oil objective (with type N immersion oil by Nikon), a Lumencore Spectra III LED (Light Emitting Diode) engine, a Perfect Focus System (PFS), temperature-controlled Okolab enclosure, and a polychroic mirror (FF-409/493/596-Di02 for by Shemrock) combined with a triple-pass emitter (FF-1-432/523/702-25 by Shemrock) for mTagBFP2/GFP/mCherry. mTagBFP2, GFP (or SYTOX Green), mCherry (or mScarlet-I) were imaged using excitation at 365 nm, 488 nm, and 594 nm, exposure of 300 ms, 200 ms, and 200 ms, and a light emitting diode (LED) power of 75%, 20%, and 30%, respectively (see (Papagiannakis et al., 2024) for power measurements for the different light sources). A 5% transmission neutral density filter was also used to lower the LED power and reduce photobleaching and phototoxicity. All experiments were carried out at 37°C unless indicated otherwise.

The microscope was controlled using NIS Elements software (Nikon), and an N-Dimensional (ND) acquisition module was used to set and acquire the time-lapse images. Phase and fluorescence images were acquired every 1 min for the single-cell and wide-trench analyses or 10 min for some of the experiments with fluorescently labeled AMPs (Figure 5C).

For experiments with PDMS microwells, cells were allowed to grow for ~30 min in the temperature-controlled enclosure prior to imaging. A 10X concentrated AMP solution was spiked in (at 1/10 the volume of the well) and mixed well by pipetting after ~20 min from the start of the image acquisition, without interrupting the timelapse sequence. When the uptake of SYTOX Green was monitored, SYTOX Green was included in the AMP solution and spiked in during the experiment to obtain a final concentration of SYTOX Green of 50 nM in the well. This allowed us to monitor healthy cell growth prior to AMP treatment, to rapidly set the desired AMP (or SYTOX Green) concentration from one frame to the next (unlike for flow-controlled injection systems), and to resolve the AMP-induced phenotype in real time. The current design allows for testing up to four independent conditions in parallel.

In 5-TAMRA-AMP enrichment experiments (Figures 5A and S7A) that used strain MG1655, unlabeled AMPs at 2X MIC were supplemented with 50 nM of the corresponding 5-TAMRA-AMP conjugate, to have an equal bulk concentration of the fluorescent label for quantifying intracellular fluorescence

increase over time. In colocalization experiments that used strains CJW7020 and CJW7859 (Figure 5C), unlabeled AMPs at concentrations equivalent to 2X MIC were supplemented with 5% of the corresponding 5-TAMRA-labeled AMP. Only for PR-39 and Bac7 and only for estimating the SCF* (Figure 5C), the labeled:unlabeled concentration ratio was increased to 25:75 and 50:50, respectively, to increase the fluorescent signal and improve the calculation of the SCF*. Selected images in Figures 5B, 5D, and S7B-E were chosen at times where both signal intensities from fluorescently labeled AMPs and cytoplasmic macromolecules (DNA or ribosomes) were the highest to aid visualization of both molecules. The different timepoints for the different fluorescently labeled AMPs or macromolecules reflect the difference in uptake kinetics or stability of the label over time (for example, HupA-msfGFP signal under Tac1 treatment exhibited a fast decay as a result of cell permeabilization).

In wide-trenches microfluidics experiments, CJW7753 or CJW7859 cells were allowed to grow for > 1 h with running fresh medium in the temperature-controlled enclosure to reach steady-state conditions prior to imaging. In experiments where strain CJW7845 was treated with rifampicin (Rif) or spectinomycin (Spect), final concentrations were both set to be 50 μg/mL.

Image processing and analysis

OmniSegger software (https://github.com/tlo-bot/omnisegger), which combines SuperSegger MATLAB-based suite (Stylianidou et al., 2016) for cell analysis with Omnipose segmentation (Cutler et al., 2022), was used to first process the microscopy images by performing drift correction, cell segmentation, and cell linking. Given that AMP-treated cells can display extreme phenotypes, such as exceedingly bright and/or heterogeneous phase contrast signal (likely a result of the widely changing intracellular density upon AMP treatment) and that the software's pre-trained model *bact_phase_omni* (Cutler et al, 2022) tended to split cells before cell division was completed, a new Omnipose model was trained from scratch starting from *bact_phase_omni*-generated masks that were further corrected and curated using custom-made Python scripts (screen_good_bad.py and generate_training_dataset.py). Details on the Omnipose model retraining can be found in a previous publication (Thappeta et al., 2024). The retrained Omnipose model can be found at https://github.com/JacobsWagnerLab/published/tree/master/Fragasso_et_al_2025.

MATLAB files of the linked cell trajectories output from OmniSegger were then imported, background subtracted using background_subtraction.py, which was adapted from a previous study (Papagiannakis et al., 2024), and converted to Python data structures (import_processing_code.py), from which cell features such as cell area, nucleoid area, mean fluorescence intensity, etc., were extracted for each cell at each frame. The exported dataframes were further processed to estimate instantaneous growth rates and were run through a series of functions to perform curation based on cell areas and instantaneous growth rates overtime (post_processing_curation_code.py). Cell trajectories (i) that were too short (< 30 min), (ii) that exhibited exceedingly large or small values in normalized (by area) instantaneous growth rate (> 0.04 min^{-1} or < -0.02 min^{-1}), (iii) whose first ten frames did not feature normal heathy growth (< 0.005 min^{-1}), or (iv) whose last ten frames did not feature growth arrest (> 0.005 min^{-1}), were removed from further analysis. In this way, only cells that exhibited healthy growth followed by growth arrest were analyzed, namely those cells for which the growth arrest-associated AMP phenotype was fully resolved. To analyze wide-trench time-lapse images, drift correction was first performed using OmniSegger, followed by a custom Python script (drift_correction_wide_trenches.py) to correct for the slow drift that was still present after the first step. Then, images were cropped, processed, and re-exported using a custom-made Python script (MM_processing.py).

Estimation of the timing of membrane permeabilization events relative to the growth rate inhibition

Analysis of strain CJW7845 proceeded by extracting the timings of permeabilization of the outer and inner membranes based on the mean fluorescence intensities of mScarlet-I and/or mTagBFP2 fluorescent proteins (using function get_permeabilization_time.py), cell growth arrest, and the initiation time of growth inhibition. To obtain accurate timings underlying membrane permeabilization events, information from both the signal intensity itself as well as its derivative were combined, which enabled us to accurately resolve the relevant changes in fluorescent protein signal beyond the intrinsic high-frequency noise and low-frequency photobleaching. Inner membrane permeabilization to proteins can result in two possible phenotypes when simultaneously monitoring freely diffusing periplasmic and cytoplasmic probes, depending on which membrane (outer or inner) becomes permeabilized first. When the outer membrane is first permeabilized, mScarlet-I signal is lost first, followed by mTagBFP2 when the inner membrane becomes also permeabilized. Conversely,

when the inner membrane is first permeabilized, mScarlet-I diffuses into the cytoplasm and mixes with mTagBFP2. To detect inner membrane permeabilization when the outer membrane remained intact (i.e., mScarlet-I leaks into the cytoplasm), the difference between periplasmic and cytoplasmic contributions of the mScarlet-I signal was computed, where periplasmic contribution corresponded to the mean fluorescence intensity of mScarlet-I within the 5-pixel thick outermost layer of the cell mask, while the cytoplasmic contribution was calculated by averaging pixel fluorescence intensities within a 7-pixel eroded mask. This way, the obtained difference $\Delta(\text{peri, cyto})_{\text{mScarlet-I}}$ remains overall positive when mScarlet-I is localized in the periplasm and becomes rapidly negative when the inner membrane becomes permeabilized as mScarlet-I diffuses into the cytoplasmic region. Detection of the permeabilization event relied on both $\Delta(\text{peri, cyto})_{\text{mScarlet-I}}$ and its normalized first derivative, which was computed by using a 5-point moving window to evaluate the local slope across the signal and dividing it by the signal itself.

When IM was permeabilized after the OM, detection of such event relied on detection of the rapid decrease of the mScarlet-I signal first (OM permeabilization), followed by the loss of the mTagBFP2 (IM permeabilization). Both signals were treated in the same way as $\Delta(\text{peri, cyto})_{\text{mScarlet-I}}$ for detecting permeabilization events, respectively, namely by using information from both the signal itself as well as their normalized first derivative.

The time marking the initiation of growth inhibition and the growth arrest were obtained by defining a multi-scale instantaneous growth rate with weights (multi_scale_derivative.py). Specifically, this function computes the weighted average of the first derivatives of differently smoothened cell areas, where these were computed using a Savitsky-Golay filter with varying moving windows. The normalized growth rate $GR_{norm}(t)$ can be expressed as

$$GR_{norm}(t) = \frac{1}{\sum_i^N w_i} \sum_{i=1}^{N} \frac{w_i}{A_{i,smooth}(t)} \frac{dA_{i,smooth}(t)}{dt}, \quad N = 5,$$

$$A_{i,smooth}(t) = SG(A(t), window_i),$$

where w_i is the ith weight, $A_{i,smooth}(t)$ is the ith smoothened area signal, SG = Savitzky-Golay filter (Savitzky & Golay, 1964) (implemented using the Python function *scipy.signal.savgol*), $window_i$ is the ith moving window size for smoothing, $A(t)$ is the original cell area signal. For the current implementation, window sizes were set to be 3, 5, 7, 9, 11, with corresponding weights 5, 8, 10, 8, 5, which were found by empirical optimization, to capture growth arrest both in the case of fast cell

shrinking events (induced by class I AMPs), where growth rate changes abruptly between one frame and the next one, as well as when growth is slowly inhibited (e.g., induced by Class II AMP treatment). As displayed in Figure S2A, the start of growth inhibition is defined as the first frame where $GR_{norm}(t) \leq 0.01$ min^{-1} and remains stably below 0.012 min^{-1} for at least 30 consecutive frames. Growth arrest is defined as the first frame where $GR_{norm}(t) \leq 0$ min^{-1} and remains stably below 0.005 min^{-1} for at least 30 consecutive frames. The use of a higher threshold to evaluate stability over consecutive frames was necessary to account for noise fluctuations of the $GR_{norm}(t)$ signal. Scatterplots presented in Figures 1F, 2C, 3D, 4C, 7C, 7G, and S8B, S8D were obtained using these different metrics.

Computation of the single-cell kymographs

To compute the kymographs (Figures 2D, 2E, 7A, 7F, and S3), a function was first used to compute the medial axis (smooth line longitudinally crossing the mid-cell) from each cell mask (get_medial_axis.py). Briefly, the medial axis was computed by first upsampling the cell mask by 20-fold in both x and y. Upon smoothing of the cell mask boundary, the Python function *skeletonize* (from *skimage.morphology*) was then used to trace the cell skeleton, which roughly corresponds to the set of pixels that are the farthest away from the cell boundary. To find the cell poles, linear regressions were fitted to the computed skeleton's extremities, specifically to the first and last three-eighths of its length, and the intersections between the extrapolated lines and the cell boundary were identified as the cell poles. Finally, a third-polynomial function was fit to the skeleton points and the poles to compute the medial axis.

Upon defining the medial axis, each cell pixel (x,y) coordinates could then be mapped into (l,d) medial axis coordinates (l = length along medial axis and d = minimum distance from medial axis; get_1D_proj_medial.py). Mean intensity projections along the medial axis length of the pixels with d < 4 pixels were computed by averaging together the pixels with the same l coordinate (kymograph_single_cell.py). Given that medial axis coordinates were computed with sub-pixel resolution using a 20X augmentation factor, the medial axis length was binned using equal bins with the original pixel size (0.065 μm/px). The resulting mean intensity projections along the medial axis length were then plotted over time to obtain the final kymographs.

Analysis of intracellular perturbations upon AMP uptake

To analyze strain CJW7753, the signal correlation factor (SCF) was computed by estimating the pixel-based Spearman correlation between the RplA-GFP and HupA-mCherry signal over a 4-pixel eroded cell mask. Exclusion of the outer 4-pixel cell layer was necessary to remove the effect of cell curvature in the proximity of the cell edge, which causes both fluorescence signals to decrease in intensity (thus causing an artefactual positive correlation). To calculate the nucleocytoplasmic (NC) ratio (= ratio between nucleoid length and cell length), a mask was applied to the HupA-mCherry signal to determine the nucleoid region (nucleoid_mask.py). Then, projections of the nucleoid pixel coordinates onto the cell medial axis were computed to estimate the arc length, namely the nucleoid length, which was obtained by calculating the Euclidean distance between consecutive pairs of pixels along the nucleoid projections. The arc length of the full medial axis, namely the cell length, was estimated using the same approach (nucleoid_cell_length.py). Cell trajectories were then aligned by the SCF peak using a multi-step alignment approach (time_alignment.py). Given that SCF signal can generally have multiple local maxima during the evolution of the phenotype after growth arrest (due to, for example, progressive loss of cell biomass, which decreases de-mixing between DNA and ribosomes, thus increasing SCF), cell trajectories for class I peptides (which featured a global peak in area that is time-associated with the SCF peak) were first aligned by peak area (here the maximum value of the area), which allowed to first roughly synchronize the trajectories by growth arrest. Then, the maximal SCF value (max SCF) within a narrow time window ($\pm$ 5-10 min) from the peak area was used to align the trajectories by the peak SCF value, resulting in all cells being synchronized by the start of their intracellular perturbations (peak SCF). For class II peptides, since the area global maximum is not generally associated with cell growth arrest, the minimum NC ratio was first used to align trajectories, then the max SCF value was searched within a narrow time window ($\pm$ 5-10 min) to obtain the peak SCF value. Given that for class II AMPs (PR-39 and Bac7), the SCF peak is broad (tens of minutes) compared to noise fluctuations, a smoothened SCF (using a 12-point moving average window) was used for both determining the peak SCF (which improved robustness against noise) and computing the ensemble curves in Figures 4B and S5. The time alignment step resulted in a new time axis that featured a SCF peak at t = 0 and which was used to generate the ensemble plots in Figures 3C, 4B, and S5. From this, the timing of peak SCF could also be extracted, which was used in the scatterplots in Figures 3D and 4C.

Analysis of fluorescently labeled AMP uptake and spatial localization

For Figures 5A and S7A, images of MG1655 cells were acquired every 1 min to enable accurate cell tracking (using OmniSegger) and probe the intracellular 5-TAMRA-AMP enrichment as a function of time aligned by the start of growth inhibition. The analysis steps for single-cell analysis were performed as explained in 'Image processing and analysis' section.

In contrast, to analyze the localization of fluorescently labeled AMPs (Figure 5C) in CJW7020 cells (expressing RplA-msfGFP) or CJW7859 cells (expressing HupA-msfGFP), images were acquired every 10 min to increase the number of fields of view, and thereby the n value, per condition since the focus of this experiment was to correlate the fluorescently labeled AMPs spatial localization with fluorescently labeled cytoplasmic macromolecules (ribosomes and DNA) after uptake, without the need to track single cells over time. For this reason, OmniSegger was used here only to perform drift correction and cell segmentation, whereas mask labeling, cropping of individual cell regions, and feature extraction were performed using a custom-made Python script (import_processing_no_linking_code.py). Since no single-cell growth rate information was obtained, the curation of badly segmented or out-of-focus cells was performed using a different strategy. First, hard thresholds on cell area removed objects that were too large (> 2000 pixels) or too small (< 500 pixels) to be cells. Second, out-of-focus cells were removed by computing the average of the pixel intensities in 40th percentile of the pixel intensities in the peripheral region of the phase contrast signal, where peripheral region corresponded to the outmost 1-pixel thick layer of the mask, computed from a 1-pixel eroded mask (the outer 1-pixel thick layer of the original mask was thus removed to avoid cell curvature effects). Third, cells that displayed low mean fluorescence values for either fluorescently labeled AMPs (< 100 a.u. for 5-TAMRA-labeled or TRITC-labeled AMPs) or msfGFP-tagged macromolecules (< 100 a.u.) were filtered out to include mostly cells that were sufficiently enriched with fluorescently labeled AMPs. To compute the spatial correlation between fluorescently labeled AMPs and the ribosomes or DNA markers (Figure 5C), a modified version of SCF (SCF*) was defined to suppress the contributions from the region of the cell where both signals were low in intensity. Starting from a 1-pixel eroded mask, pixel-based Spearman correlation was computed between the pixel intensities in the 50th percentile of both channels. The resulting SCF* appears to represent more strongly the visually observed anti-colocalization between fluorescently labeled AMPs and the DNA marker HupA-msfGFP, while providing positive correlation values when the signals are colocalized (as reported in Figure 5C for SCF* between fluorescently labeled AMPs

and the ribosome marker RplA-msfGFP). The timepoints for evaluating the SCF* were chosen based on having a sufficiently high signal for both fluorescent reporters. The timepoints (relative to addition of the AMP mixture) were 10 min, 50 min, 100 min, 50 min, 30 min, 40 min, and 80 min, for 5-TAMRA-CecA, 5-TAMRA-Tac1, 5-TAMRA-LL-37, TRITC-LL-37, 5-TAMRA-PR-39, 5-TAMRA-Bac7, and 5-TAMRA-DJK-5, respectively, for RplA-msfGFP-expressing CJW7020, and 0 min (first frame after AMP addition), 50 min, 100 min, 50 min, 30 min, 40 min, and 80 min, for 5-TAMRA-CecA, 5-TAMRA-Tac1, 5-TAMRA-LL-37, TRITC-LL-37, 5-TAMRA-PR-39, 5-TAMRA-Bac7, and 5-TAMRA-DJK-5, respectively, for HupA-msfGFP-expressing strain CJW7859.

Calculation of correlation coefficients

All Spearman's correlations, used for SCF and SCF* calculations, were computed using the Python function *spearmanr* from *scipy.stats* library.

Analysis software, hardware, code, and data availability

Drift correction and cell linking using SuperSegger code (https://github.com/tlo-bot/omnisegger) were performed using MATLAB (www.mathworks.com). Repository for using the Omnipose deep neural network architecture (Cutler et al., 2022) was downloaded from https://github.com/kevinjohncutler/omnipose.git and installed in a local Miniconda environment.

Omnipose retraining, segmentation, and computationally intensive tasks that involved operations on large arrays (background_subtraction.py; medial_axis.py) were accelerated by parallel processing on an NVIDIA A40 GPU utilizing CUDA (Compute Unified Device Architecture) to enhance performance. All the custom-written code was developed using Python 3.9 (www.python.org). The following packages were employed in the analysis: *numpy* (Harris et al., 2020), *cupy* (Okuta et al., 2017), *pytorch* (Paszke et al., 2019), *pandas* (McKinney, 2010), *scipy* (Virtanen et al., 2020), *matplotlib* (Hunter, 2007), *seaborn* (Waskom, 2021), *scikit-learn* (Pedregosa et al., 2011), *scikit-image* (Walt et al., 2014). The analysis pipeline and functions can be found in the Jacobs-Wagner laboratory Github repository (https://github.com/JacobsWagnerLab/published/tree/master/Fragasso_et_al_2025). The microscopy images used in this study are available on BioStudies and the BioImage Archive (accession number: S-BIAD1823).

ACKNOWLEDGEMENTS

We are grateful to Drs. Silvia Cañas-Duarte and Johan Paulsson for the gift of the periplasmic-mScarlet-I reporter construct and Dr. Johan Paulsson for also sharing the design for the three-dimensional-printed holder used in this study. We thank Dr K. Prather (Massachusetts Institute of Technology) for the MG1655 (DE3) strain. We also thank Dr. Alexandros Papagiannakis for his gift of strain CJW7753. In addition, we are grateful to the members of the Jacobs-Wagner laboratory for fruitful discussions, support, and critical reading of the manuscript. This work was supported in part by a Director's Pioneer Award (# 1DP1 OD029517) from The National Institute of Aging (to A.E.B.), funding from the SENS Foundation and Dr. James J. Truchard and the Truchard Foundation (to A.E.B.), and the Netherlands Organization for Scientific Research (research program Rubicon 2022-2 Science programme, 019.222EN.001804 to A.F.). A.E.B. acknowledges work at the Molecular Foundry supported by the Office of Science, Office of Basic Energy Sciences, of the U.S. Department of Energy under Contract No. DE-AC02-05CH11231. C.J.W. is an investigator of the Howard Hughes Medical Institute.

AUTHOR CONTRIBUTIONS

Conceptualization, A.F., A.E.B., and C.J.-W.; methodology, A.F., T.S., W.-H.L.; software, A.F.; formal analysis, A.F.; investigation, A.F.; resources, A.F. , A.E.B., W.-H.L., and C.J.-W.; data curation, A.F.; writing – original draft, A.F. and C.J.-W.; writing – review and editing, A.F., T.S., A.E.B., C.J.-W ; visualization, A.F. and C.J.-W.; supervision, C.J.-W.; project administration, C.J.-W.; funding acquisition, A.F., A.E.B, and C.J.-W.

DECLARATION OF INTERESTS

The authors declare no competing interests.

REFERENCES

Bakshi, S., Siryaporn, A., Goulian, M., & Weisshaar, J. C. (2012). Superresolution imaging of ribosomes and RNA polymerase in live *Escherichia coli* cells. *Molecular Microbiology*, *85*(1), 21–38. https://doi.org/10.1111/j.1365-2958.2012.08081.x

Balleza, E., Kim, J. M., & Cluzel, P. (2018). Systematic characterization of maturation time of fluorescent proteins in living cells. *Nature Methods*, *15*(1), 47–51. https://doi.org/10.1038/nmeth.4509

Benn, G., Pyne, A. L. B., Ryadnov, M. G., & Hoogenboom, B. W. (2019). Imaging live bacteria at the nanoscale: Comparison of immobilisation strategies. *Analyst*, *144*(23), 6944–6952. https://doi.org/10.1039/C9AN01185D

Bevis, B. J., & Glick, B. S. (2002). Rapidly maturing variants of the Discosoma red fluorescent protein (DsRed). *Nature Biotechnology*, *20*(1), 83–87. https://doi.org/10.1038/nbt0102-83

Boeynaems, S., Ma, X. R., Yeong, V., Ginell, G. M., Chen, J.-H., Blum, J. A., Nakayama, L., Sanyal, A., Briner, A., Van Haver, D., Pauwels, J., Ekman, A., Schmidt, H. B., Sundararajan, K., Porta, L., Lasker, K., Larabell, C., Hayashi, M. A. F., Kundaje, A., ... Gitler, A. D. (2023). *Aberrant phase separation is a common killing strategy of positively charged peptides in biology and human disease* [Preprint]. Cell Biology. https://doi.org/10.1101/2023.03.09.531820

Boman, H. G., Agerberth, B., & Boman, A. (1993). Mechanisms of action on Escherichia coli of cecropin P1 and PR-39, two antibacterial peptides from pig intestine. *Infection and Immunity*, *61*(7), 2978–2984.

Cañas-Duarte, S. J., & J, S. (2021). *Understanding rare events in Escherichia coli*. https://nrs.harvard.edu/URN-3:HUL.INSTREPOS:37368226

Cardoso, M. H., Meneguetti, B. T., Costa, B. O., Buccini, D. F., Oshiro, K. G. N., Preza, S. L. E., Carvalho, C. M. E., Migliolo, L., & Franco, O. L. (2019). Non-lytic antibacterial peptides that

translocate through bacterial membranes to act on intracellular targets. *International Journal of Molecular Sciences*, *20*(19). https://doi.org/10.3390/ijms20194877

Cherepanov, P. P., & Wackernagel, W. (1995). Gene disruption in *Escherichia coli*: TcR and KmR cassettes with the option of Flp-catalyzed excision of the antibiotic-resistance determinant. *Gene*, *158*(1), 9–14. https://doi.org/10.1016/0378-1119(95)00193-A

Choi, H., Rangarajan, N., & Weisshaar, J. C. (2016). Lights, Camera, Action! Antimicrobial Peptide Mechanisms Imaged in Space and Time. *Trends in Microbiology*, *24*(2), 111–122. https://doi.org/10.1016/j.tim.2015.11.004

Chongsiriwatana, N. P., Lin, J. S., Kapoor, R., Wetzler, M., Rea, J. A. C., Didwania, M. K., Contag, C. H., & Barron, A. E. (2017). Intracellular biomass flocculation as a key mechanism of rapid bacterial killing by cationic, amphipathic antimicrobial peptides and peptoids. *Scientific Reports*, *7*(1), 1–15. https://doi.org/10.1038/s41598-017-16180-0

Chongsiriwatana, N. P., Patch, J. A., Czyzewski, A. M., Dohm, M. T., Ivankin, A., Gidalevitz, D., Zuckermann, R. N., & Barron, A. E. (2008). Peptoids that mimic the structure, function, and mechanism of helical antimicrobial peptides. *Proceedings of the National Academy of Sciences of the United States of America*, *105*(8), 2794–2799. https://doi.org/10.1073/pnas.0708254105

Chung, C. T., Niemela, S. L., & Miller, R. H. (1989). One-step preparation of competent Escherichia coli: Transformation and storage of bacterial cells in the same solution. *Proceedings of the National Academy of Sciences*, *86*(7), 2172–2175. https://doi.org/10.1073/pnas.86.7.2172

Costerton, J. W., Stewart, P. S., & Greenberg, E. P. (1999). Bacterial Biofilms: A Common Cause of Persistent Infections. *Science*, *284*(5418), 1318–1322. https://doi.org/10.1126/science.284.5418.1318

Cutler, K. J., Stringer, C., Lo, T. W., Rappez, L., Stroustrup, N., Brook Peterson, S., Wiggins, P. A., & Mougous, J. D. (2022). Omnipose: A high-precision morphology-independent solution for bacterial cell segmentation. *Nature Methods*, *19*(11), 1438–1448. https://doi.org/10.1038/s41592-022-01639-4

Datsenko, K. A., & Wanner, B. L. (2000). One-step inactivation of chromosomal genes in Escherichia coli K-12 using PCR products. *Proceedings of the National Academy of Sciences*, *97*(12), 6640–6645. https://doi.org/10.1073/pnas.120163297

De La Fuente-Núñez, C., Reffuveille, F., Haney, E. F., Straus, S. K., & Hancock, R. E. W. (2014). Broad-Spectrum Anti-biofilm Peptide That Targets a Cellular Stress Response. *PLoS Pathogens*, *10*(5), e1004152. https://doi.org/10.1371/journal.ppat.1004152

De La Fuente-Núñez, C., Reffuveille, F., Mansour, S. C., Reckseidler-Zenteno, S. L., Hernández, D., Brackman, G., Coenye, T., & Hancock, R. E. W. (2015). D-Enantiomeric Peptides that Eradicate Wild-Type and Multidrug-Resistant Biofilms and Protect against Lethal Pseudomonas aeruginosa Infections. *Chemistry & Biology*, *22*(2), 196–205. https://doi.org/10.1016/j.chembiol.2015.01.002

Ghosh, A., Kar, R. K., Jana, J., Saha, A., Jana, B., Krishnamoorthy, J., Kumar, D., Ghosh, S., Chatterjee, S., & Bhunia, A. (2014). Indolicidin Targets Duplex DNA: Structural and Mechanistic Insight through a Combination of Spectroscopy and Microscopy. *ChemMedChem*, *9*(9), 2052–2058. https://doi.org/10.1002/cmdc.201402215

Gray, W. T., Govers, S. K., Xiang, Y., Parry, B. R., Campos, M., Kim, S., & Jacobs-Wagner, C. (2019). Nucleoid Size Scaling and Intracellular Organization of Translation across Bacteria. *Cell*, *177*(6), 1632-1648.e20. https://doi.org/10.1016/j.cell.2019.05.017

Hale, J. D., & Hancock, R. E. (2007). Alternative mechanisms of action of cationic antimicrobial peptides on bacteria. *Expert Review of Anti-Infective Therapy*, *5*(6), 951–959. https://doi.org/10.1586/14787210.5.6.951

Hancock, R. E. W., Haney, E. F., & Gill, E. E. (2016). The immunology of host defence peptides: Beyond antimicrobial activity. *Nature Reviews Immunology*, *16*(5), 321–334. https://doi.org/10.1038/nri.2016.29

Harris, C. R., Millman, K. J., van der Walt, S. J., Gommers, R., Virtanen, P., Cournapeau, D., Wieser, E., Taylor, J., Berg, S., Smith, N. J., Kern, R., Picus, M., Hoyer, S., van Kerkwijk, M. H., Brett, M., Haldane, A., del Río, J. F., Wiebe, M., Peterson, P., … Oliphant, T. E. (2020). Array programming with NumPy. *Nature*, *585*(7825), 357–362. https://doi.org/10.1038/s41586-020-2649-2

Hebisch, E., Knebel, J., Landsberg, J., Frey, E., & Leisner, M. (2013). High Variation of Fluorescence Protein Maturation Times in Closely Related Escherichia coli Strains. *PLoS ONE*, *8*(10), e75991. https://doi.org/10.1371/journal.pone.0075991

Hsu, C.-H. (2005). Structural and DNA-binding studies on the bovine antimicrobial peptide, indolicidin: Evidence for multiple conformations involved in binding to membranes and DNA. *Nucleic Acids Research*, *33*(13), 4053–4064. https://doi.org/10.1093/nar/gki725

Huang, W., Baliga, C., Aleksandrova, E. V., Atkinson, G., Polikanov, Y. S., Vázquez-Laslop, N., & Mankin, A. S. (2024). Activity, structure, and diversity of Type II proline-rich antimicrobial peptides from insects. *EMBO Reports*, *25*(11), 5194–5211. https://doi.org/10.1038/s44319-024-00277-5

Hunter, J. D. (2007). Matplotlib: A 2D Graphics Environment. *Computing in Science & Engineering*, *9*(3), 90–95. Computing in Science & Engineering. https://doi.org/10.1109/MCSE.2007.55

Johansson, J., Gudmundsson, G. H., Rottenberg, M. E., Berndt, K. D., & Agerberth, B. (1998). Conformation-dependent Antibacterial Activity of the Naturally Occurring Human Peptide LL-37. *Journal of Biological Chemistry*, *273*(6), 3718–3724. https://doi.org/10.1074/jbc.273.6.3718

Kostakioti, M., Hadjifrangiskou, M., & Hultgren, S. J. (2013). Bacterial Biofilms: Development, Dispersal, and Therapeutic Strategies in the Dawn of the Postantibiotic Era. *Cold Spring Harbor Perspectives in Medicine*, *3*(4), a010306–a010306. https://doi.org/10.1101/cshperspect.a010306

Kyte, J., & Doolittle, R. F. (1982). A simple method for displaying the hydropathic character of a protein. *Journal of Molecular Biology*, *157*(1), 105–132. https://doi.org/10.1016/0022-2836(82)90515-0

Lambert, G., & Kussell, E. (2014). Memory and Fitness Optimization of Bacteria under Fluctuating Environments. *PLoS Genetics*, *10*(9), e1004556. https://doi.org/10.1371/journal.pgen.1004556

Le, C.-F., Fang, C.-M., & Sekaran, S. D. (2017). Intracellular Targeting Mechanisms by Antimicrobial Peptides. *Antimicrobial Agents and Chemotherapy*, *61*(4), 1–16.

Lewis, P. J., Thaker, S. D., & Errington, J. (2000). Compartmentalization of transcription and translation in Bacillus subtilis. *The EMBO Journal*, *19*(4), 710–718. https://doi.org/10.1093/emboj/19.4.710

Li, X., Zuo, S., Wang, B., Zhang, K., & Wang, Y. (2022). Antimicrobial Mechanisms and Clinical Application Prospects of Antimicrobial Peptides. *Molecules*, *27*(9), 2675. https://doi.org/10.3390/molecules27092675

Lin, W.-H., & Jacobs-Wagner, C. (2022). Connecting single-cell ATP dynamics to overflow metabolism, cell growth, and the cell cycle in Escherichia coli. *Current Biology*, *32*(18), 3911-3924.e4. https://doi.org/10.1016/j.cub.2022.07.035

Linnik, D., Maslov, I., Punter, C. M., & Poolman, B. (2024). Dynamic structure of E. coli cytoplasm: Supramolecular complexes and cell aging impact spatial distribution and mobility of proteins. *Communications Biology*, *7*(1), 508. https://doi.org/10.1038/s42003-024-06216-3

Liu, H., Song, Z., Zhang, Y., Wu, B., Chen, D., Zhou, Z., Zhang, H., Li, S., Feng, X., Huang, J., & Wang, H. (2025). De novo design of self-assembling peptides with antimicrobial activity guided by deep learning. *Nature Materials*, 1–12. https://doi.org/10.1038/s41563-025-02164-3

Luo, Y., & Song, Y. (2021). Mechanism of Antimicrobial Peptides: Antimicrobial, Anti-Inflammatory and Antibiofilm Activities. *International Journal of Molecular Sciences*, *22*(21), 11401. https://doi.org/10.3390/ijms222111401

Mardirossian, M., Pérébaskine, N., Benincasa, M., Gambato, S., Hofmann, S., Huter, P., Müller, C., Hilpert, K., Innis, C. A., Tossi, A., & Wilson, D. N. (2018). The Dolphin Proline-Rich Antimicrobial Peptide Tur1A Inhibits Protein Synthesis by Targeting the Bacterial Ribosome. *Cell Chemical Biology*, *25*(5), 530-539.e7. https://doi.org/10.1016/j.chembiol.2018.02.004

Mattiuzzo, M., Bandiera, A., Gennaro, R., Benincasa, M., Pacor, S., Antcheva, N., & Scocchi, M. (2007). Role of the *Escherichia coli* SbmA in the antimicrobial activity of proline-rich peptides. *Molecular Microbiology*, *66*(1), 151–163. https://doi.org/10.1111/j.1365-2958.2007.05903.x

McKinney, W. (2010). Data Structures for Statistical Computing in Python. *Proceedings of the 9th Python in Science Conference*, 56–61. https://doi.org/10.25080/Majora-92bf1922-00a

Megerle, J. A., Fritz, G., Gerland, U., Jung, K., & Rädler, J. O. (2008). Timing and Dynamics of Single Cell Gene Expression in the Arabinose Utilization System. *Biophysical Journal*, *95*(4), 2103–2115. https://doi.org/10.1529/biophysj.107.127191

Mookherjee, N., Anderson, M. A., Haagsman, H. P., & Davidson, D. J. (2020). Antimicrobial host defence peptides: Functions and clinical potential. *Nature Reviews Drug Discovery*, *19*(5), 311–332. https://doi.org/10.1038/s41573-019-0058-8

Okuta, R., Unno, Y., Nishino, D., Hido, S., & Loomis, C. (2017). *CuPy: A NumPy-Compatible Library for NVIDIA GPU Calculations*. 31st Conference on Neural Information Processing Systems (NIPS 2017), Long Beach, CA, USA.

Oren, Z., Lerman, J. C., Gudmundsson, G. H., Agerberth, B., & Shai, Y. (1999). *Structure and organization of the human antimicrobial peptide LL-37 in phospholipid membranes: Relevance to the molecular basis for its non-cell-selective activity*.

Papagiannakis, A., Yu, Q., Govers, S. K., Lin, W.-H., Wingreen, N. S., & Jacobs-Wagner, C. (2024). *Nonequilibrium polysome dynamics promote chromosome segregation and its coupling to cell growth in* Escherichia coli. https://doi.org/10.1101/2024.10.08.617237

Paszke, A., Gross, S., Massa, F., Lerer, A., Bradbury, J., Chanan, G., Killeen, T., Lin, Z., Gimelshein, N., Antiga, L., Desmaison, A., Köpf, A., Yang, E., DeVito, Z., Raison, M., Tejani, A., Chilamkurthy, S., Steiner, B., Fang, L., … Chintala, S. (2019). PyTorch: An imperative style, high-performance deep learning library. In *Proceedings of the 33rd International Conference on Neural Information Processing Systems* (pp. 8026–8037). Curran Associates Inc.

Pedregosa, F., Varoquaux, G., Gramfort, A., Michel, V., Thirion, B., Grisel, O., Blondel, M., Prettenhofer, P., Weiss, R., Dubourg, V., Vanderplas, J., Passos, A., Cournapeau, D., Brucher, M., Perrot, M., & Duchesnay, É. (2011). Scikit-learn: Machine Learning in Python. *J. Mach. Learn. Res.*, *12*(null), 2825–2830.

Peschel, A., & Sahl, H.-G. (2006). The co-evolution of host cationic antimicrobial peptides and microbial resistance. *Nature Reviews Microbiology*, *4*(7), 529–536. https://doi.org/10.1038/nrmicro1441

Podda, E., Benincasa, M., Pacor, S., Micali, F., Mattiuzzo, M., Gennaro, R., & Scocchi, M. (2006). Dual mode of action of Bac7, a proline-rich antibacterial peptide. *Biochimica Et Biophysica Acta*, *1760*(11), 1732–1740. https://doi.org/10.1016/j.bbagen.2006.09.006

Pränting, M., Negrea, A., Rhen, M., & Andersson, D. I. (2008). Mechanism and Fitness Costs of PR-39 Resistance in *Salmonella enterica* Serovar Typhimurium LT2. *Antimicrobial Agents and Chemotherapy*, *52*(8), 2734–2741. https://doi.org/10.1128/AAC.00205-08

Roth, B. L., Poot, M., Yue, S. T., & Millard, P. J. (1997). Bacterial viability and antibiotic susceptibility testing with SYTOX green nucleic acid stain. *Applied and Environmental Microbiology*, *63*(6), 2421–2431. https://doi.org/10.1128/aem.63.6.2421-2431.1997

Sanamrad, A., Persson, F., Lundius, E. G., Fange, D., Gynnå, A. H., & Elf, J. (2014). Single-particle tracking reveals that free ribosomal subunits are not excluded from the *Escherichia coli* nucleoid. *Proceedings of the National Academy of Sciences*, *111*(31), 11413–11418. https://doi.org/10.1073/pnas.1411558111

Savitzky, Abraham., & Golay, M. J. E. (1964). Smoothing and Differentiation of Data by Simplified Least Squares Procedures. *Analytical Chemistry*, *36*(8), 1627–1639. https://doi.org/10.1021/ac60214a047

Schavemaker, P. E., Śmigiel, W. M., & Poolman, B. (2017). Ribosome surface properties may impose limits on the nature of the cytoplasmic proteome. *eLife*, *6*, e30084. https://doi.org/10.7554/eLife.30084

Scocchi, M., Lüthy, C., Decarli, P., Mignogna, G., Christen, P., & Gennaro, R. (2009). The Proline-rich Antibacterial Peptide Bac7 Binds to and Inhibits in vitro the Molecular Chaperone DnaK.

International Journal of Peptide Research and Therapeutics, *15*(2), 147–155. https://doi.org/10.1007/s10989-009-9182-3

Scocchi, M., Tossi, A., & Gennaro, R. (2011). Proline-rich antimicrobial peptides: Converging to a non-lytic mechanism of action. *Cellular and Molecular Life Sciences*, *68*(13), 2317–2330. https://doi.org/10.1007/s00018-011-0721-7

Sharan, S. K., Thomason, L. C., Kuznetsov, S. G., & Court, D. L. (2009). Recombineering: A homologous recombination-based method of genetic engineering. *Nature Protocols*, *4*(2), 206–223. https://doi.org/10.1038/nprot.2008.227

Sneideris, T., Erkamp, N. A., Ausserwöger, H., Saar, K. L., Welsh, T. J., Qian, D., Katsuya-Gaviria, K., Johncock, M. L. L. Y., Krainer, G., Borodavka, A., & Knowles, T. P. J. (2023). Targeting nucleic acid phase transitions as a mechanism of action for antimicrobial peptides. *Nature Communications*, *14*(1), 7170. https://doi.org/10.1038/s41467-023-42374-4

Snoussi, M., Talledo, J. P., Del Rosario, N. A., Mohammadi, S., Ha, B. Y., Košmrlj, A., & Taheri-Araghi, S. (2018). Heterogeneous absorption of antimicrobial peptide LL37 in escherichia coli cells enhances population survivability. *eLife*, *7*, 1–21. https://doi.org/10.7554/eLife.38174

Stylianidou, S., Brennan, C., Nissen, S. B., Kuwada, N. J., & Wiggins, P. A. (2016). SuperSegger: Robust image segmentation, analysis and lineage tracking of bacterial cells. *Molecular Microbiology*, *102*(4), 690–700. https://doi.org/10.1111/mmi.13486

Subach, O. M., Cranfill, P. J., Davidson, M. W., & Verkhusha, V. V. (2011). An Enhanced Monomeric Blue Fluorescent Protein with the High Chemical Stability of the Chromophore. *PLoS ONE*, *6*(12), e28674. https://doi.org/10.1371/journal.pone.0028674

Subbalakshmi, C., & Sitaram, N. (1998). Mechanism of antimicrobial action of indolicidin. *FEMS Microbiology Letters*, *160*(1), 91–96. https://doi.org/10.1111/j.1574-6968.1998.tb12896.x

Svenson, J., Molchanova, N., & Schroeder, C. I. (2022). Antimicrobial Peptide Mimics for Clinical Use: Does Size Matter? *Frontiers in Immunology*, *13*, 915368. https://doi.org/10.3389/fimmu.2022.915368

Taheri-Araghi, S. (2024). Synergistic action of antimicrobial peptides and antibiotics: Current understanding and future directions. *Frontiers in Microbiology*, *15*, 1390765. https://doi.org/10.3389/fmicb.2024.1390765

Thappeta, Y., Cañas-Duarte, S. J., Kallem, T., Fragasso, A., Xiang, Y., Gray, W., Lee, C., Cegelski, L., & Jacobs-Wagner, C. (2024). *Glycogen phase separation drives macromolecular rearrangement and asymmetric division in* E. coli. https://doi.org/10.1101/2024.04.19.590186

Thomason, L. C., Costantino, N., & Court, D. L. (2007). E. coli genome manipulation by P1 transduction. *Current Protocols in Molecular Biology*, *Chapter 1*, 1.17.1-1.17.8. https://doi.org/10.1002/0471142727.mb0117s79

Virtanen, P., Gommers, R., Oliphant, T. E., Haberland, M., Reddy, T., Cournapeau, D., Burovski, E., Peterson, P., Weckesser, W., Bright, J., van der Walt, S. J., Brett, M., Wilson, J., Millman, K. J., Mayorov, N., Nelson, A. R. J., Jones, E., Kern, R., Larson, E., ... van Mulbregt, P. (2020). SciPy 1.0: Fundamental algorithms for scientific computing in Python. *Nature Methods*, *17*(3), 261–272. https://doi.org/10.1038/s41592-019-0686-2

Walt, S. van der, Schönberger, J. L., Nunez-Iglesias, J., Boulogne, F., Warner, J. D., Yager, N., Gouillart, E., & Yu, T. (2014). scikit-image: Image processing in Python. *PeerJ*, *2*, e453. https://doi.org/10.7717/peerj.453

Wan, F., Wong, F., Collins, J. J., & De La Fuente-Nunez, C. (2024). Machine learning for antimicrobial peptide identification and design. *Nature Reviews Bioengineering*, *2*(5), 392–407. https://doi.org/10.1038/s44222-024-00152-x

Wang, G., Li, X., & Wang, Z. (2016). APD3: The antimicrobial peptide database as a tool for research and education. *Nucleic Acids Research*, *44*(D1), D1087–D1093. https://doi.org/10.1093/nar/gkv1278

Wang, G., Zietz, C. M., Mudgapalli, A., Wang, S., & Wang, Z. (2022). The evolution of the antimicrobial peptide database over 18 years: Milestones and new features. *Protein Science*, *31*(1), 92–106. https://doi.org/10.1002/pro.4185

Waskom, M. L. (2021). seaborn: Statistical data visualization. *Journal of Open Source Software*, *6*(60), 3021. https://doi.org/10.21105/joss.03021

Wimley, W. C., & Hristova, K. (2011). Antimicrobial peptides: Successes, challenges and unanswered questions. *Journal of Membrane Biology*, *239*(1–2), 27–34. https://doi.org/10.1007/s00232-011-9343-0

Xiang, Y., Surovtsev, I. V., Chang, Y., Govers, S. K., Parry, B. R., Liu, J., & Jacobs-Wagner, C. (2021). Interconnecting solvent quality, transcription, and chromosome folding in Escherichia coli. *Cell*, *184*(14), 3626--3642.e14. https://doi.org/10.1016/j.cell.2021.05.037

Yonezawa, A., Kuwahara, J., Fujii, N., & Sugiura, Y. (1992). Binding of tachyplesin I to DNA revealed by footprinting analysis: Significant contribution of secondary structure to DNA binding and implication for biological action. *Biochemistry*, *31*(11), 2998–3004. https://doi.org/10.1021/bi00126a022

Zhu, Y., Mohapatra, S., & Weisshaar, J. C. (2019). Rigidification of the Escherichia coli cytoplasm by the human antimicrobial peptide LL-37 revealed by superresolution fluorescence microscopy. *Proceedings of the National Academy of Sciences of the United States of America*, *116*(3), 1017–1026. https://doi.org/10.1073/pnas.1814924116

Zuckermann, R. N., Kerr, J. M., Kent, S. B. H., & Moos, W. H. (1992). Efficient method for the preparation of peptoids [oligo(N-substituted glycines)] by submonomer solid-phase

synthesis. *Journal of the American Chemical Society*, *114*(26), 10646–10647.

https://doi.org/10.1021/ja00052a076

FIGURE LEGENDS

Figure 1: AMPs can be classified based on the phenotypes they cause at the temporal and single-cell resolution. (A) List of natural AMPs and synthetic mimics used in this study. Also shown are their features and minimal inhibitory concentrations (MIC) at which no growth of *E. coli* (MG1655) could be detected after incubation in M9gluCAAT at 37°C for 20 h, starting with an inoculum of ~250 cells/mL (see Figure S1A for the MIC results). Some peptides have disulfide bonds (Cys-Cys) and/or an amide group (-NH_2) at their C-terminal end, as indicated. Peptide structures were obtained from the Protein Data Bank or the AlphaFold Protein Structure Database (PDB: 5HAU, 1KJ6, 1G8C, 5NMN, 2MAG, 2MLT, 2RTV, 6FKR; AlphaFold: AF-P01507-F1, AF-P80054-F1). The asterisk indicates that the peptide DJK-5 is composed of D-amino acids. **(B)** Plots showing how the selected AMPs vary in sequence-specific characteristics thought to be important for their antibacterial activities. Some data are difficult to see because they overlap; see Table S1 for a complete set of numerical values. **(C)** Cell schematic of the *E. coli* strain (CJW7845) used to examine the permeabilization of the inner and outer membranes to the indicated fluorescent proteins in response to AMP exposure. **(D)** Plot showing SYTOX Green uptake over time since the addition of different AMPs at concentrations equivalent to 2X MIC. Control antibiotics Rif and Spect were present at a final concentration of 50 μg/mL. The left plot shows the full range of measured SYTOX Green values. The right plot shows a zoom-in to visualize the results for the AMPs for which SYTOX Green uptake was lower. The total number of cells was 101, 180, 299, 175, 159, 103, 116, 179, 176, 142, 111, 142 for CecA, Tac1, Mag2, LL-37, Mltt, HBD-3, Indo, PR-39, Bac7, Tur1A, Rif, and Spect, respectively. **(E)** Plot showing the cumulative distribution of inner membrane (IM) permeabilization times for different AMPs and control antibiotics as a function of time since AMP or antibiotic addition, using the same set of treated cells as in (D). The total number of IM-permeabilized cells examined was 99, 177, 290, 162, 143, 77, 93, 109, 23, 10, 2, and 3 for CecA, Tac1, Mag2, LL-37, Mltt, HBD-3, Indo, PR-39, Bac7, Tur1A, Rif, and Spect, respectively**. (F)** Scatterplots showing the time of growth arrest since AMP addition vs. that of IM permeabilization since AMP addition across the AMPs. The total number of cells for

each AMP is the same as in (E). The dashed line indicates $y = x$. Opacity of each data point was set to 15% to aid visualization of the data density. By definition, AMPs were classified based on whether the growth arrest that they cause is predominantly associated with IM permeabilization to proteins (class I, red) or not (class II, blue).

Figure 2: Class I AMPs can be subdivided into types A and B based on the relative timing of permeabilization of each membrane. (A) Schematics showing what happens to the cytoplasmic mTagBFP2 and periplasmic mScarlet-I for each class I AMP type. By definition, type A predominantly permeabilizes the outer membrane (OM) of cells simultaneously with, or before, the inner membrane (IM), resulting in the release of both mScarlet-I and mTagBFP2 into the environment. In contrast, type B primarily permeabilizes the IM well before the OM (which may or may not permeabilize during the experiment, see panel B), resulting in the mixing of mScarlet-I and mTagBFP2 within the OM boundaries. **(B)** Plot showing the cumulative distribution of OM permeabilization events for different class I AMPs used at concentrations equivalent to their 2X MICs (Figure 1A). Here, only cells for which the IM became permeabilized during the experiment were considered. They represent 99/99, 177/177, 290/290, 162/162, 72/143, 9/77, and 0/93 cells for CecA, Tac1, Mag2, LL-37, Mltt, HBD-3, and Indo, respectively. **(C)** Scatterplots showing the time of OM permeabilization since AMP addition as a function of IM permeabilization since AMP addition across the AMPs. Opacity of each data point was set to 25% to aid visualization of the data density. The dashed line indicates $y = x$. **(D**) Example kymographs of mScarlet-I and mTagBFP2 signals for a representative CJW7845 cell exposed with CecA (1 μM) at the indicated time. The times of IM and OM permeabilizations are shown. See also Video 1. **(E)** Same as (D) but for a cell treated with Indo (25 μM). See also Video 2. **(F)** Plots showing the quantification of the cell length and fluorescence signal (top) and the difference $\Delta(\text{peri,cyto})_{\text{mScarlet-I}}$ between the mScarlet-I signal in the cell periphery (periplasm) relative to the cell interior (cytoplasm) over time for the cell shown in panel (D). **(G)** Same as (F) except for the cell shown in (E).

Figure 3. The growth arrest by class I AMPs is associated with a fast reorganization of ribosomes and DNA inside cells. (A) Cell schematic of strain CJW7753 expressing mTagBFP2, RplA-GFP, and HupA-mCherry as markers for cytoplasmic proteins, ribosomes, and DNA, respectively. **(B)** Images

of a representative CJW7753 cell at the indicated specific timepoints (h:min) illustrating changes in intracellular ribosome and DNA distributions. CecA (1 μM, 2X MIC) was added at 19 min. See Video 3 for the whole time-lapse sequence. **(C)** Plots showing the quantification of the evolution of the mean ± 95% confidence interval (CI) of the cell length, signal correlation factor (SCF), nucleocytoplasmic (NC) ratio, and mTagBFP2 fluorescence (fluor.) across 314 cells. Times were aligned based on the SCF peak in each cell (indicated by the black dashed line). **(D)** Scatterplots showing the time of SCF peak as a function of the time of growth arrest across the indicated class I AMPs (2X MIC). The total number of cells is 314, 117, 103, 172, 102, 53, and 152 for CecA, Tac1, Mag2, LL-37, Mltt, HBD-3, and Indo, respectively. Opacity of each data point was set to 15% to aid visualization of the data density. The dashed line indicates $y = x$.

Figure 4. The initiation of growth inhibition by class II AMPs is associated with a slow reorganization of ribosomes and DNA inside cells. (A) Images of a representative CJW7753 cell at the indicated specific timepoints (h:min) illustrating changes in intracellular ribosome and DNA distributions. PR-39 (4 μM, 2X MIC) was added at 18 min. See Video 4 for the whole time-lapse sequence. **(B)** Plots showing the quantification of the evolution of the mean ± 95% confidence interval (CI) of the cell length, smoothened signal correlation factor (SCF), nucleocytoplasmic (NC) ratio, and mTagBFP2 fluorescence (fluor.) across 180 cells. Times were aligned based on the smoothened SCF peak at the single-cell level. The black dashed line indicates the smoothened SCF peak (time zero). **(C)** Scatterplots showing the time of SCF peak as a function of the start of growth inhibition for the indicated class II AMPs. The total number of cells is 180, 61, and 138 for PR-39, Bac7, and Tur1A (2X MIC), respectively. Opacity of each data point was set to 15% to aid visualization of the data density. The dashed line indicates $y = x$.

Figure 5. The intracellular distribution of fluorescent AMP derivatives correlates with the ribosome signal and anti-correlates with the DNA signal. (A) Evolution of the intracellular fluorescence intensity (mean ± 95 % CI) of 5-TAMRA-AMP conjugates, present at 50 nM together with the corresponding unlabeled AMPs (2X MIC) in MG1655 cells. Time axis of each single cell was aligned by start time of growth inhibition. The total number of averaged cells is 138, 116, 101, 125, 254, 180, for CecA, Tac1, LL-37, PR-39, Bac7, and DJK-5, respectively. **(B)** *Top*, representative images

of the indicated fluorescence signal in CJW7020 cells (expressing RplA-msfGFP) exposed to a mixture of Tac1 (1.2 μM, 2X MIC) and 5-TAMRA-Tac1 (60 nM, 5% of the unlabeled version) for 50 min. *Bottom*, representative images of the indicated fluorescence signal in CJW7859 cells (expressing HupA-msfGFP) exposed to a mixture of Tac1 (1.2 μM, 2X MIC) and 5-TAMRA-Tac1 (60 nM, 5% of the unlabeled version) for 20 min. See STAR Methods for explanation about the timepoint selection. **(C)** Plot showing mean ± 95 % CI of the signal correlation factor (SCF*, which is slightly modified version of SCF, see STAR Methods) between the fluorescently labeled AMP signal and the RplA-msfGFP (black circles) or HupA-msfGFP (grey squares) fluorescent signal. CJW7020 and CJW7859 cells (expressing RplA-msfGFP or HupA-msfGFP, respectively) were treated with a mixture of CecA (1 μM, 2X MIC), Tac1 (1.2 μM, 2X MIC), LL-37 (2 μM, 2X MIC), PR-39 (3 μM, 1.5X MIC), Bac7 (1.2 μM, 2X MIC), and DJK-5 (5 μM, 2X MIC), plus 5% (or 33% for PR-39, 100% for Bac7) of the corresponding fluorescently labeled version, which resulted in the final concentrations of 50 nM 5-TAMRA-CecA, 60 nM 5-TAMRA-Tac1, 100 nM 5-TAMRA-LL-37, 100 nM TRITC-LL-37, 1 μM 5-TAMRA-PR-39, 1.2 μM 5-TAMRA-Bac7, and 250 nM 5-TAMRA-DJK-5, respectively. See STAR Methods for the timepoint selection. The total number of cells for CJW7020 was 1358 for 5-TAMRA-CecA, 726 for 5-TAMRA-Tac1, 623 for 5-TAMRA-LL-37, 585 for TRITC-LL-37, 135 for 5-TAMRA-PR-39, 2512 for 5-TAMRA-Bac7, and 369 for 5-TAMRA-DJK-5. For CJW7859 the number of cells was 566 for 5-TAMRA-CecA, 375 for 5-TAMRA-Tac1, 480 for 5-TAMRA-LL-37, 233 for TRITC-LL-37, 191 for 5-TAMRA-PR-39, 1001 for 5-TAMRA-Bac7, and 176 for 5-TAMRA-DJK-5. **(D)** Same as (B) except that the selected CJW7020 cell expressing RplA-msfGFP (top) CJW7859 cell expressing HupA-msfGFP (bottom) treated with a 75:25 mixture of PR-39 (3 μM, 1.5X MIC) and 5-TAMRA-PR-39 (1 μM, 33% of the unlabeled version) were permeabilized, enhancing the intracellular uptake and absorption of PR-39 and its fluorescent derivative. See STAR Methods for the timepoint selection.

Figure 6. Class I AMPs are less effective against high cell densities than class II peptides. (A) Schematics illustrating the AMP release by a mammalian gut epithelium (left) and a neutrophil (right). Adapted from a BioRender template (BioRender.com). **(B)** Schematic of the wide-trench microfluidic device. Purple arrow indicates the polarized delivery of AMPs to emulate the in vivo situations illustrated in (A). **(C)** Representative images of CJW7753 cells (expressing RplA-GFP and HupA-mCherry) in a wide trench when either LL-37 (2 μM, 2X MIC), Indo (25 μM, 2X MIC), or PR-39 (4 μM, 2X MIC) are present in the medium flowed in the feeding channel. See Videos 5, 10, 11 for the whole

time-lapse sequences. **(D)** Representative images of CJW7859 cells (expressing HupA-msfGFP) growing at 30°C instead of 37°C when the medium contains 20 μM (20X MIC) LL-37. The two selected timepoints illustrate how LL-37-absorbing cells at the top of the trench are pushed out by the growing cells below. Video 14 shows a whole time-lapse sequence for two representative cell-filled trenches.

Figure 7. Phenotype-based classification applies to synthetic AMP mimics TM1 and DJK-5. (A) Example kymographs showing the evolution of the mScarlet-I and mTagBFP2 signals for a representative CJW7845 cell exposed with peptoid TM1 (5 μM, 2X MIC). **(B)** Plot showing the cumulative distribution of the fraction of IM-permeabilized cells treated with TM1 (5 μM, 2X MIC) and DJK-5 (5 μM, 2X MIC)**.** The total number of IM-permeabilized cells is 82 for TM1 and 132 for DJK-5. **(C)** Scatterplot showing the time of growth arrest since AMP addition *vs*. that of inner membrane (IM) permeabilization since AMP addition for cells treated with peptoid TM1 (5 μM, 2X MIC). The total number of cells is 82. Opacity of each data point was set to 15% to aid visualization of the data density. The dashed line indicates $y = x$**.** **(D)** Plot showing the cumulative distribution of the fraction of OM-permeabilized cells among the IM-permeabilized population during treatment with TM1 (5 μM, 2X MIC) or DJK-5 (5 μM, 2X MIC)**.** The total number of cells was 15 for TM1 and 53 for DJK-5. **(E)** Representative images of CJW7753 cells (expressing RplA-GFP and HupA-mCherry) in a wide trench when TM1 (5 μM, 2X MIC) is present in the medium flowed in the feeding channel. See Video 15 for the whole time-lapse sequence. **(F)** Same as (A) but for DJK-5 treatment (5 μM, 2X MIC). **(G)** Same as (B) but for DJK-5. The total number of cells is 132. **(H)** Representative images of CJW7753 cells (expressing RplA-GFP and HupA-mCherry) in a wide trench when DJK-5 (5 μM, 2X MIC) is present in the medium flowed in the feeding channel. See Video 16 for the whole time-lapse sequence.

SUPPLEMENTARY FIGURE LEGENDS

Figure S1: Features relevant to the experimental approach. (A) Plots showing maximum growth rate (log(OD)/h) at varying concentrations of peptide (or peptoid) for the different AMPs used in this study, extracted from OD_{600} measurements using a microplate reader (see the Methods section for details). The color bar indicates the time at which the maximum growth rate was detected over the course of the measurement. Black markers indicate the concentrations for which the maximum growth rate was < 0.2 log(OD)/h, where the leftmost black marker corresponds to the minimum

inhibitory concentration (MIC). **(B)** Schematic of the multi-well device used to image cells. **(C)** Representative images of the mScarlet-I signal in CJW7845 cells. **(D)** Same as (A) but for the indicated fluorescently labeled AMPs.

Figure S2: Determination of growth arrest, start of growth inhibition, and residuals of (IM permeabilization, growth arrest) times from *y* = *x*. (A) Example trajectories of cell area (black) and normalized growth rate (red, as defined in STAR Methods) for a cell treated with CecA (left) or PR-39 (right). Horizontal grey dotted and black dashed lines indicate hard thresholds used for detection of start of growth inhibition or growth arrest, respectively. Vertical grey dotted and black dashed lines indicate the identified times of start of growth inhibition and growth arrest, respectively, using the definitions written on the right. **(B)** Absolute residuals of times of growth arrest since AMP addition vs. times of IM permeabilization since AMP addition from the diagonal ($y = x$), for the indicated AMPs (same dataset used in Figure 1F).

Figure S3: Example kymographs of mScarlet-I and mTagBFP2 signals for CJW7845 cells upon exposure to HBD-3, PR-39, Bac7, and Tur1A. (A) Top: Example kymographs of mScarlet-I and mTagBFP2 signals for a representative CJW7845 cell exposed with HBD-3 (20 μM, 2X MIC) at the indicated time. The times of IM and OM permeabilizations are shown. Bottom: Plots showing the quantification of the cell length and fluorescence signal (top) and the difference $\Delta(\text{peri,cyto})_{\text{mScarlet-I}}$ between the mScarlet-I signal in the cell periphery (periplasm) relative to the cell interior (cytoplasm) over time for cell shown above. **(B)** Same as (A) but for PR-39 (4 μM, 2X MIC). **(C)** Same as (A) but for Bac7 (1.2 μM, 2X MIC). **(D)** Same as (A) but for Tur1A (1 μM, 2X MIC).

Figure S4: SYTOX Green uptake in CJW7845 cells relative to the initiation time of growth inhibition. Plot showing SYTOX Green uptake *vs* time relative to initiation time of growth inhibition for different AMPs at concentrations equivalent to their 2X MICs (see Figure 1A). The left plot shows the full range of measured SYTOX Green values. The right plot shows a zoom-in to visualize the AMPs for which SYTOX Green uptake was lower. The total number of cells was 101, 180, 299, 175, 159, 103, 116, 179, 176, 142, 111, 142 for CecA, Tac1, Mag2, LL-37, Mltt, HBD-3, Indo, PR-39, Bac7, Tur1A, Rif, and Spect, respectively.

Figure S5: Quantification of the intracellular DNA and ribosome reorganization upon Bac7 and Tur1A treatment. (A) Plots showing the quantification of the evolution of the mean ± 95% confidence interval (CI) of the cell length, signal correlation factor (SCF), nucleocytoplasmic (NC) ratio, and mTagBFP2 fluorescence (fluor.) across 61 cells exposed to Bac7 (1.2 μM, 2X MIC). Times were aligned based on the SCF peak at the single-cell level. The black dashed line indicates the SCF peak (time zero). **(B)** Same as (A) but for Tur1A (1 μM, 2X MIC). The number of cells was 138.

Figure S6: Quantification of the time delay between AMP addition and growth arrest for CecA, LL-37, Mltt, Bac7, and PR-39 across different peptide concentrations relative to their MICs. Plot showing the time delay between AMP addition and growth arrest for CJW7753 cells treated with the shown AMPs at the indicated concentrations relative to their MICs (shown in Figure 1A). The total number of cells for the following conditions is indicated in parenthesis: for CecA at 1X MIC (47), 2X MIC (316), and 10X MIC (98); for LL-37 at 1X MIC (31), 2X MIC (203), and 10X MIC (63), for Mltt at 1X MIC (40), 2X MIC (110), and 10X MIC (67); for PR-39 at 1X MIC (135), 2X MIC (183), and 10X MIC (34); and for Bac7 at 1X MIC (213), 2X MIC (65), 10X MIC (107).

Figure S7: Intracellular enrichment and spatial localization of fluorescently labeled AMPs. (A) Intracellular fluorescence intensity (mean± 95 % CI) of 5-TAMRA conjugates to the indicated AMPs 10 min after their addition for MG1655 strain (same data as in Figure 5A) present at 50 nM together with the corresponding unlabeled AMPs (2X MIC) in MG1655 cells. Time is relative to the start time of growth inhibition. The total number of averaged cells is 138, 116, 101, 125, 254, 180, for CecA, Tac1, LL-37, PR-39, Bac7, and DJK-5, respectively. **(B)** Top: Representative images of the indicated fluorescence signal in CJW7020 cells (expressing RplA-msfGFP, top) or CJW7859 (expressing HupA-msfGFP, bottom) exposed to a mixture of CecA (1 μM, 2X MIC) and 5-TAMRA-CecA (50 nM, 5% of the unlabeled version) for 10 min or 20 min, respectively. **(C)** Same as (B) except that cells were exposed to a mixture of LL-37 (2 μM, 2X MIC) and 100 nM (5% of the unlabeled version) of 5-TAMRA-LL-37 for 50 min. **(D)** Same as (C) except the fluorescent LL-37 derivative was TRITC-LL-37 and the exposure was for 60 min. **(E)** Same as (B) except that cells were exposed to a mixture of DJK-5 (5 μM, 2X MIC) and 5-TAMRA-DJK-5 (250 nM, 5% of the unlabeled version) for 5 h and 40 min (for CJW7020 cell, top) or 3 h and 10 min (for CJW7859 cells, bottom).

Figure S8: Example single-cell trajectories and timing of outer vs inner membrane permeabilization for peptoid TM1 and D-enantiomeric peptide DJK-5. (A) Plots of the cell length, normalized mean fluorescence signals of mScarlet-I and mTagBFP2, and difference $\Delta(\text{peri,cyto})_{\text{mScarlet-I}}$ between the mScarlet-I fluorescence signal in the cell periphery (periplasm) relative to the cell interior (cytoplasm) over time, for the cell represented in Figure 7A, treated with TM1 (5 μM, 2X MIC). **(B)** Scatterplot showing the time of OM permeabilization as a function of the time of IM permeabilization for CJW7845 cells exposed with TM1 (5 μM, 2X MIC). The total number of OM-permeabilized cells (out of all IM-permeabilized cells) was 15/82. Opacity of each data point was set to 25% to aid the visualization of the data density. The dashed line indicates $y = x$. **(C)** Same as (A) but for the cell represented in Figure 7F, treated with DJK-5 (5 μM, 2X MIC). **(D)** Scatterplot showing the time of OM permeabilization as a function of the time of IM permeabilization for CJW7845 cells exposed with DJK-5 (5 μM, 2X MIC). The total number of OM-permeabilized cells (out of all IM-permeabilized cells) was 53. The opacity of each data point was set to 25% to aid the visualization of the data density. The dashed line indicates $y = x$.

TABLE LEGENDS

Table S1: Physicochemical properties of the selected AMPs. Data underlying scatterplots shown in Figure 1B for each AMP or peptidomimetic described in Figure 1A.

VIDEO LEGENDS

Video 1: Timelapse sequence showing inner and outer membrane permeabilization to proteins upon CecA treatment. Montage video showing phase contrast, mScarlet-I fluorescence, mTagBFP2 fluorescence, and SYTOX Green fluorescence in the top row of a representative CJW7845 cell under treatment with 1 μM (2X MIC) CecA. SYTOX Green signal is plotted using a low and a high dynamic range (DR) of intensity values to enable visualization at both low- and high-intensity values, respectively. Time stamp shows h:min. The scale bar is 1 μm. The bottom row shows extracted cell parameters (cell length and mean intensities for each fluorescent probe) over time for the same cell. The red dashed line indicates the time of CecA addition. The black dotted line indicates the time at which the cell reaches the maximum length prior to cell shrinkage.

Video 2: Timelapse sequence showing inner membrane permeabilization to proteins upon Indo treatment. Montage video showing phase contrast, mScarlet-I fluorescence, mTagBFP2 fluorescence, and SYTOX Green fluorescence in the top row of a representative CJW7845 cell under treatment with 25 μM (2X MIC) Indo. SYTOX Green signal is displayed both with adjusted high brightness (high br.) and low brightness (low br.) to enable visualization at both low and high intensity values, respectively. The time stamp shows h:min. The scale bar is 1 μm. The bottom row shows extracted cell parameters (cell length and mean intensities for each fluorescent probe) over time for the same cell. The red dashed line indicates the time of Indo addition. The black dotted line indicates the time at which the cell reaches the maximum length prior to cell shrinkage.

Video 3: Timelapse sequence showing intracellular DNA and ribosome reorganization upon CecA treatment. Montage video showing phase contrast, RplA-GFP, HupA-mCherry, and mTagBFP2 fluorescence in the top row of a representative CJW7753 cell under treatment with 1 μM (2X MIC) CecA. The time stamp shows h:min. The scale bar is 1 μm. The bottom row shows plots of cell length, signal correlation factor (SCF), nucleocytoplasmic (NC) ratio, and mean mTagBFP2 intensity. The red dashed line indicates the time of CecA addition. The black dotted line indicates the time at which the cell reaches the maximum length prior to cell shrinkage.

Video 4: Timelapse sequence showing DNA and ribosome reorganization upon PR-39 treatment. Montage video showing phase contrast, RplA-GFP, HupA-mCherry, and mTagBFP2 fluorescence in the top row of a representative CJW7753 cell under treatment with 4 μM (2X MIC) PR-39. The time stamp shows h:min. The scale bar is 1 μm. The bottom row shows plots of cell length, signal correlation factor (SCF), nucleocytoplasmic (NC) ratio, and mean mTagBFP2 intensity. The red line indicates the time of PR-39 addition.

Video 5: Timelapse sequence showing the poor killing activity of LL-37 against a dense population of *E. coli* cells in a wide trench. Montage video showing phase contrast, RplA-GFP, and HupA-mCherry fluorescence of CJW7753 cells in a representative wide trench under treatment with LL-37 at 2 μM, which corresponds to 2X MIC at low cell density (Figure 1A). Time stamp shows h:min.

the scale bar is 5 μm. The red label appearance indicates the time when the medium containing 2 μM of LL-37 was started to be flown through the microfluidic system.

Video 6: Timelapse sequence showing the poor killing activity of CecA against a dense population of *E. coli* cells in a wide trench. Montage video showing phase contrast, RplA-GFP, and HupA-mCherry fluorescence of CJW7753 cells in a representative wide trench under treatment with CecA at 1 μM, which corresponds to 2X MIC at low cell density (Figure 1A). Time stamp shows h:min. The scale bar is 5 μm. The red label appearance indicates the time when the medium containing 1 μM of CecA started to be flown through the microfluidic system.

Video 7: Timelapse sequence showing the poor killing activity of Tac1 against a dense population of *E. coli* cells in a wide trench. Montage video showing phase contrast, RplA-GFP, and HupA-mCherry fluorescence of CJW7753 cells in a representative wide trench under treatment with Tac1 at 1.2 μM, which corresponds to 2X MIC at low cell density (Figure 1A). Time stamp shows h:min. The scale bar is 5 μm. The red label appearance indicates the time when the medium containing 1.2 μM of Tac1 started to be flown through the microfluidic system.

Video 8: Timelapse sequence showing the poor killing activity of Mag2 against a dense population of *E. coli* cells in a wide trench. Montage video showing phase contrast, RplA-GFP, and HupA-mCherry fluorescence of CJW7753 cells in a representative wide trench under treatment with Mag2 at 40 μM, which corresponds to 2X MIC at low cell density (Figure 1A). Time stamp shows h:min. The scale bar is 5 μm. The red label appearance indicates the time when the medium containing 40 μM of Mag2 started to be flown through the microfluidic system.

Video 9: Timelapse sequence showing the poor killing activity of Mltt against a dense population of *E. coli* cells in a wide trench. Montage video showing phase contrast, RplA-GFP, and HupA-mCherry fluorescence of CJW7753 cells in a representative wide trench under treatment with Mltt at 8 μM, which corresponds to 2X MIC at low cell density (Figure 1A). Time stamp shows h:min. The

scale bar is 5 μm. The red label appearance indicates the time when the medium containing 8 μM of Mltt started to be flown through the microfluidic system.

Video 10: Timelapse sequence showing the poor killing activity of Indo against a dense population of *E. coli* cells in a wide trench. Montage video showing phase contrast, RplA-GFP, and HupA-mCherry fluorescence of CJW7753 cells in a representative wide trench under treatment with Indo at 25 μM, which corresponds to 2X MIC at low cell density (Figure 1A). Time stamp shows h:min. The scale bar is 5 μm. The red label appearance indicates the time when the medium containing 25 μM of Indo was started to be flown through the microfluidic system.

Video 11: Timelapse sequence showing the ability of PR-39 to inhibit the growth of a dense population of *E. coli* cells in a wide trench. Montage video showing phase contrast, RplA-GFP, and HupA-mCherry fluorescence of CJW7753 cells in a representative wide trench under treatment with PR-39 at 4 μM, which corresponds to 2X MIC at low cell density (Figure 1A). The time stamp shows h:min. The scale bar is 5 μm. The red label appearance indicates the time when the medium containing 4 μM of PR-39 was started to be flown through the microfluidic system.

Video 12: Timelapse sequence showing the ability of Bac7 to inhibit the growth of a dense population of *E. coli* cells in a wide trench. Montage video showing phase contrast, RplA-GFP, and HupA-mCherry fluorescence of CJW7753 cells in a representative wide trench under treatment with Bac7 at 1.2 μM, which corresponds to 2X MIC at low cell density (Figure 1A). The time stamp shows h:min. The scale bar is 5 μm. The red label appearance indicates the time when the medium containing 1.2 μM of Bac7 was started to be flown through the microfluidic system.

Video 13: Timelapse sequence showing the ability of Tur1A to inhibit the growth of a dense population of *E. coli* cells in a wide trench. Montage video showing phase contrast, RplA-GFP, and HupA-mCherry fluorescence of CJW7753 cells in a representative wide trench under treatment with Tur1A at 1 μM, which corresponds to 2X MIC at low cell density (Figure 1A). The time stamp shows

h:min. The scale bar is 5 μm. The red label appearance indicates the time when the medium containing 1μM of Tur1A was started to be flown through the microfluidic system.

Video 14: Timelapse sequence showing the high cell absorption and poor killing activity of a high concentration of LL-37 in a wide trench containing a dense *E. coli* cell population growing at 30°C. Montage video showing LL-37 fluorescence, along with the phase contrast and HupA-msfGFP signals of CJW7859 cells in a representative wide trench under treatment with 20 μM LL-37 (which corresponds to 20X MIC at low cell density, see Figure 1A) at 30°C. The third empty trench is shown to showcase the diffusion of LL-37 across the wide trench. Time stamp shows h:min. The scale bar is 5 μm. The red label appearance indicates the time when the medium containing 20 μM of LL-37 was started to be flown through the microfluidic system.

Video 15: Timelapse sequence showing the poor killing activity of TM1 against a dense population of *E. coli* cells in a wide trench. Montage video showing phase contrast, RplA-GFP, and HupA-mCherry fluorescence of CJW7753 cells in a representative wide trench under treatment with TM1 at 5 μM, which corresponds to 2X MIC at low cell density (Figure 1A). The time stamp shows h:min. The scale bar is 5 μm. The red label appearance indicates the time when the medium containing 5 μM of Tm1 was started to be flown through the microfluidic system.

Video 16: Timelapse sequence showing the ability of DJK-5 to inhibit the growth of a dense *E. coli* cell population in a wide trench. Montage video showing phase contrast, RplA-GFP, and HupA-mCherry fluorescence of CJW7753 cells in a representative wide trench under treatment with DJK-5 at 5 μM, which corresponds to 2X MIC at low cell density (Figure 1A). The time stamp shows h:min. The scale bar is 5 μm. The red label appearance indicates the time when the medium containing 5 μM of DJK-5 was started to be flown through the microfluidic system.

RESOURCE OR REAGENT	SOURCE	IDENTIFIER
Bacterial strains		
E. coli MG1655 (F- lambda- *ilvG- rfb-50 rph-1*)	(Guyer et al., 1981; Jensen, 1993)	MG1655
E. coli MG1655 Tn7::*pRNA1-ssDsbA-mScarlet-I-rrnB1T1-frt-CmR-frt*	(Cañas-Duarte & J, 2021)	SJC164
E. coli DH5α λpir+ / *pKD13-msfgfp*	(Gray et al., 2019)	CJW6871
E. coli MG1655 *rplA*::*rplA-msfgfp*	(Gray et al., 2019)	CJW7020
E. coli MG1655 *hupA*::*hupA-mcherry rplA*::*rplA-gfp*	(Xiang et al., 2021)	CJW7323
E. coli MG1655 *hupA*::*hupA-mcherry rplA*::*rplA-gfp* / pBAD-mtagbfp2	This study	CJW7753
E. coli MG1655 Tn7::*pRNA1-ssDsbA-mScarlet-I-rrnB1T1-frt-CmR-frt* / pBAD-mtagbfp2	This study	CJW7845
E. coli MG1655 *hupA*::*hupA-msfgfp*	This study	CJW7859
Recombinant DNA / plasmids		
(Gly-Ser)x3-msfgfp-frt-kanR-frt-repR6K-ampR	(Gray et al., 2019)	pKD13-msfgfp
λ-repressor(Ts)-bet-exo-repA101(Ts)-ampR	National Cancer Institute https://ncifrederick.cancer.gov/recombineering/strains-plasmids-and-primers	pSim6
araC-ParaBAD-mTagBFP2-ampRpBAD322ori	(Subach et al., 2011)	pBAD-mTagBFP2
cmR-repA101(Ts)-ampR-flp-λ-repressor(Ts)	(Datsenko and Wanner, 2000)	pCP20
Oligonucleotides		
5'-GGCATTTGTTTCTGGCAAGGCACTGAAAGACGCAGTTAAGGGCAGCGGCAGCGGCAGCTC-3'	This study	HU_msfGFP_rev
5'-AAACCACCCCTTCGTTAAAACTGTTCACTGCCACGCAATCATCCGTCGACCTGCAGTTCG-3'	This study	HU_msfGFP_for
5'-TGTCGTACCTGGAGTCTTCC-3'	This study	hupA_seq_for
5'-TTCAGCAAATCCACTGGCGG-3'	This study	hupA_seq_rev
Chemicals, peptides and probes		
SYTOX™ Green Nucleic Acid Stain - 5 mM Solution in DMSO	Thermo Fisher Scientific	Cat# S7020
LL-37	AnaSpec Inc.	Cat# AS-61302
Human β-defensin 3	AnaSpec Inc.	Cat# AS-60741
Magainin 2	AnaSpec Inc.	Cat# AS-20639
Cecropin A	AnaSpec Inc.	Cat# AS-24009
Indolicidin	AnaSpec Inc.	Cat# AS-60999
PR-39	Abbiotec	Cat# 350590
Tachyplesin I	Bachem AG	Cat# 4030734
Bactenecin-7	NovoPro Bioscience Inc.	Cat# 318782
Tur1A	NovoPro Bioscience Inc.	Cat# 318733
DJK-5	NovoPro Bioscience Inc.	Cat# 318921
5-TAMRA-CecA	NovoPro Bioscience Inc.	Custom design
5-TAMRA-LL-37	NovoPro Bioscience Inc.	Custom design
5-TAMRA-Tac1	NovoPro Bioscience Inc.	Custom design
5-TAMRA-PR-39	NovoPro Bioscience Inc.	Custom design
5-TAMRA-Bac7	NovoPro Bioscience Inc.	Custom design
5-TAMRA-DJK-5	NovoPro Bioscience Inc.	Custom design
TRITC-LL-37	Rockland Immunochemicals, Inc.	Cat# 000-000-M33
Spectinomycin	Sigma Aldrich	Cat# S9007
Rifampicin	Sigma Aldrich	Cat# R3501
L-Arabinose	Spectrum Chemical	Cat# AR110-100GM
Software and algorithms		
www.github.com/tlo-bot/omnisegger	(Cutler et al., 2022; Stylianidou et al., 2016)	OmniSegger
www.mathworks.com	Mathworks	MATLAB
www.python.org	Python Software Foundation	Python
www.numpy.org	(Harris et al., 2020)	Numpy
www.scipy.org	(Virtanen et al., 2020)	Scipy
www.pytorch.org	(Paszke et al., 2019)	Pytorch
www.scikit-image.org	(Van Der Walt et al., 2014)	Scikit-image
www.scikit-learn.org/stable/	(Pedregosa et al., 2012)	Scikit-learn
https://cupy.dev/	(Okuta et al., 2017)	Cupy
www.pypi.org/project/shapely/	(Gillies, Sean et al., 2023)	Shapely
www.matplotlib.org	(Hunter, 2007)	Matplotlib

www.seaborn.pydata.org	(Waskom, 2021)	Seaborn
www.pandas.pydata.org	(McKinney, 2010)	Pandas
Importing and processing cell trajectories output from OmniSegger for single-cell analysis	This study (www.github.com/JacobsWagnerLab/published/tree/master/Fragasso_et_al_2025)	import_processing_code.py
Importing and processing cell masks output from Omnipose segmentation for population-level analysis	This study (www.github.com/JacobsWagnerLab/published/tree/master/Fragasso_et_al_2025)	import_processing_code_no_linking.py
Functions for single-cell analysis and feature extraction	This study (www.github.com/JacobsWagnerLab/published/tree/master/Fragasso_et_al_2025)	analysis_functions_library.py
Background subtraction	This study (www.github.com/JacobsWagnerLab/published/tree/master/Fragasso_et_al_2025)	background_subtraction.py
Medial axis computation from cell masks	This study (www.github.com/JacobsWagnerLab/published/tree/master/Fragasso_et_al_2025)	get_medial_axis.py
Mean intensity projection of the pixel intensities onto medial axis	This study (www.github.com/JacobsWagnerLab/published/tree/master/Fragasso_et_al_2025)	get_1D_proj_medial.py
Kymograph computation from mean intensity projections	This study (www.github.com/JacobsWagnerLab/published/tree/master/Fragasso_et_al_2025)	kymograph_single_cell.py
Compute nucleoid mask	This study (www.github.com/JacobsWagnerLab/published/tree/master/Fragasso_et_al_2025)	nucleoid_mask.py
Compute nucleoid arc length from medial axis and nucleoid mask	This study (www.github.com/JacobsWagnerLab/published/tree/master/Fragasso_et_al_2025)	nucleoid_length.py
Extraction of timings of permeabilization of inner and outer membranes	This study (www.github.com/JacobsWagnerLab/published/tree/master/Fragasso_et_al_2025)	get_permeabilization_time.py
Estimation of normalized growth rate for calculation of growth parameters	This study (www.github.com/JacobsWagnerLab/published/tree/master/Fragasso_et_al_2025)	multi_scale_derivative.py
Additional functions for post-processing and curation of single-cell trajectories	This study (www.github.com/JacobsWagnerLab/published/tree/master/Fragasso_et_al_2025)	post_processing_curation_code.py
Function to perform time alignment of single-cell trajectories based on extracted cell features (area and SCF)	This study (www.github.com/JacobsWagnerLab/published/tree/master/Fragasso_et_al_2025)	time_alignment.py
Function to perform drift-correction of wide-trench microfluidics timelapse sequences	This study (www.github.com/JacobsWagnerLab/published/tree/master/Fragasso_et_al_2025)	drift_correction_wide_trenches.py
Importing, processing, and plotting of wide-trenches microfluidics timelapse sequences	This study (www.github.com/JacobsWagnerLab/published/tree/master/Fragasso_et_al_2025)	MM_processing.py

Figure 1

A

Name (abbreviation)	Sequence	Source	Structure	Cys-Cys	C-terminal NH_2	MIC (μM)
Bactenecin-7 (Bac7)	RRIRPRPPRLPRPRPRPLPFPRPGPRPIPRPLPFP	Bovine	extended	0	No	0.6
Cecropin A (CecA)	KWKLFKKIEKVGQNIRDGIIKAGPAVAVVGQATQIAK	Moth	α-helix with hinge	0	Yes	0.5
Human β-defensin 3 (HBD-3)	GIINTLQKYYCRVRGGRCAVLSCLPKEEQIGKCSTRGRKCCRRKK	Human	β-sheet	3	No	10.0
Indolicidin (Indo)	ILPWKWPWWPWRR	Bovine	extended	0	Yes	12.5
LL-37	LLGDFFRKSKEKIGKEFKRIVQRIKDFLRNLVPRTES	Human	α-helix	0	No	1
Magainin-2 (Mag2)	GIGKFLHSAKKFGKAFVGEIMNS	Frog	α-helix	0	No	20
Melittin (Mltt)	GIGAVLKVLTTGLPALISWIKRKRQQ	Honey bee	α-helix	0	Yes	4.0
PR-39	RRRPRPPYLPRPRPPPFFPPRLPPRIPPGFPPRFPPRFP	Porcine	extended	0	Yes	2.0
Tachyplesin-1 (Tac1)	KWCFRVCYRGICYRRCR	Horseshoe crab	β-hairpin	2	Yes	0.6
Tur1A	RRIRFRPPYLPRPGRRPRFPPPFPIPRIPRIP	Cetacean	extended	0	No	0.5
DJK-5	VQWRAIRVRVIR*	Synthetic	unknown	0	Yes	2.5

B

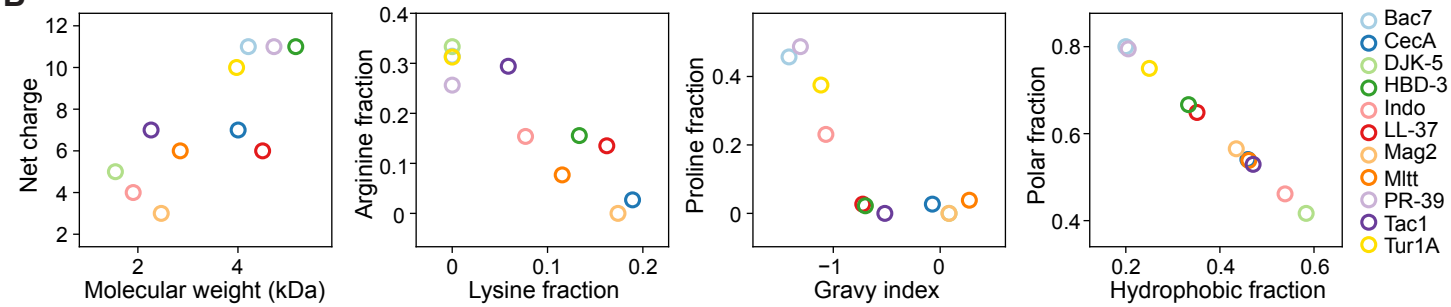

C

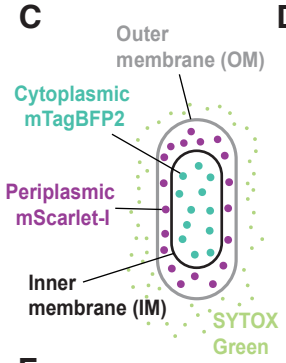

D

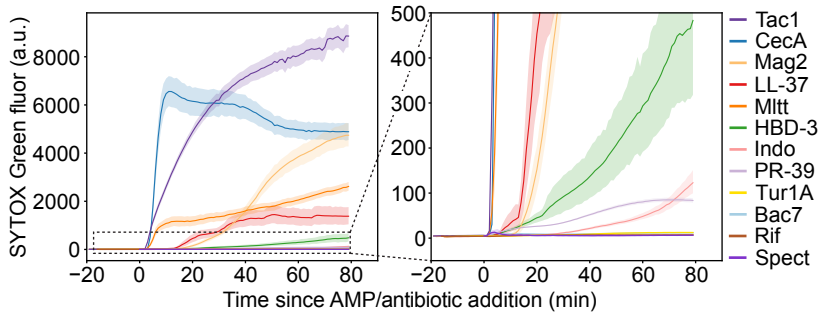

E

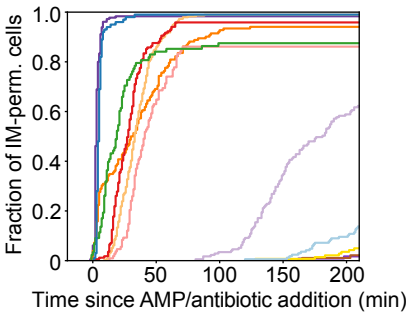

F

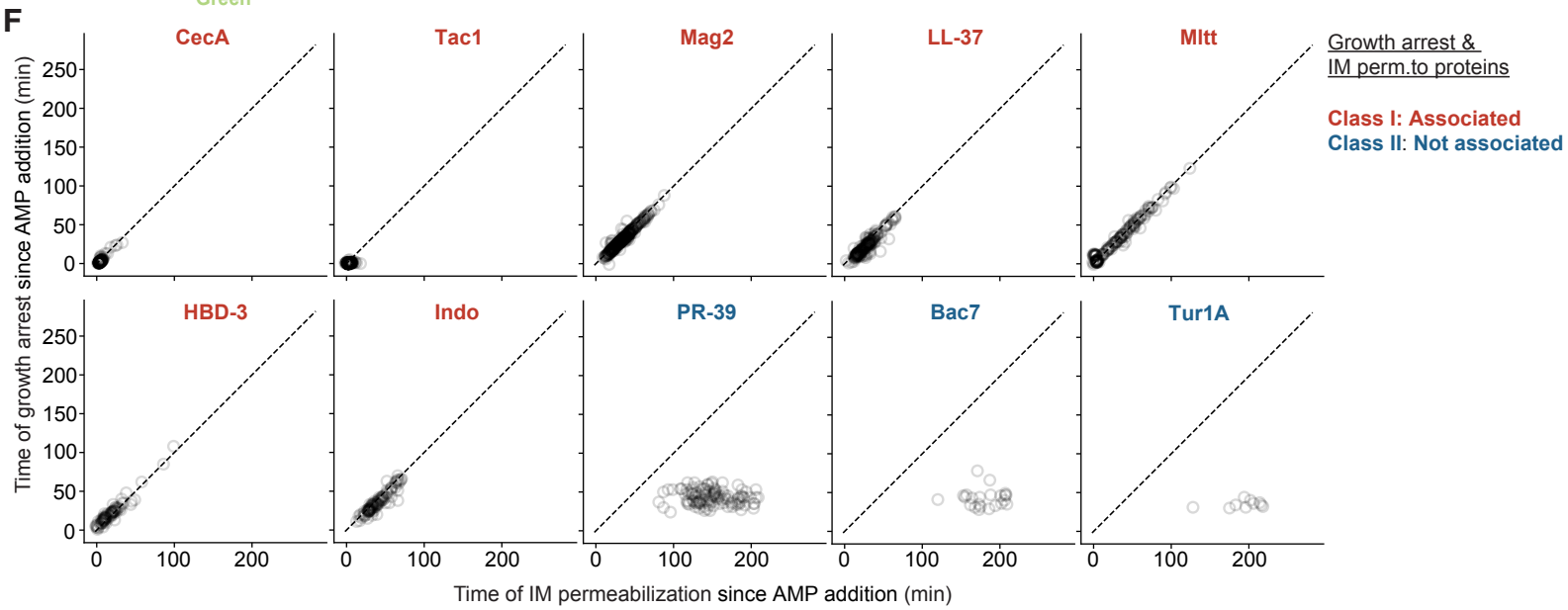

Figure 2

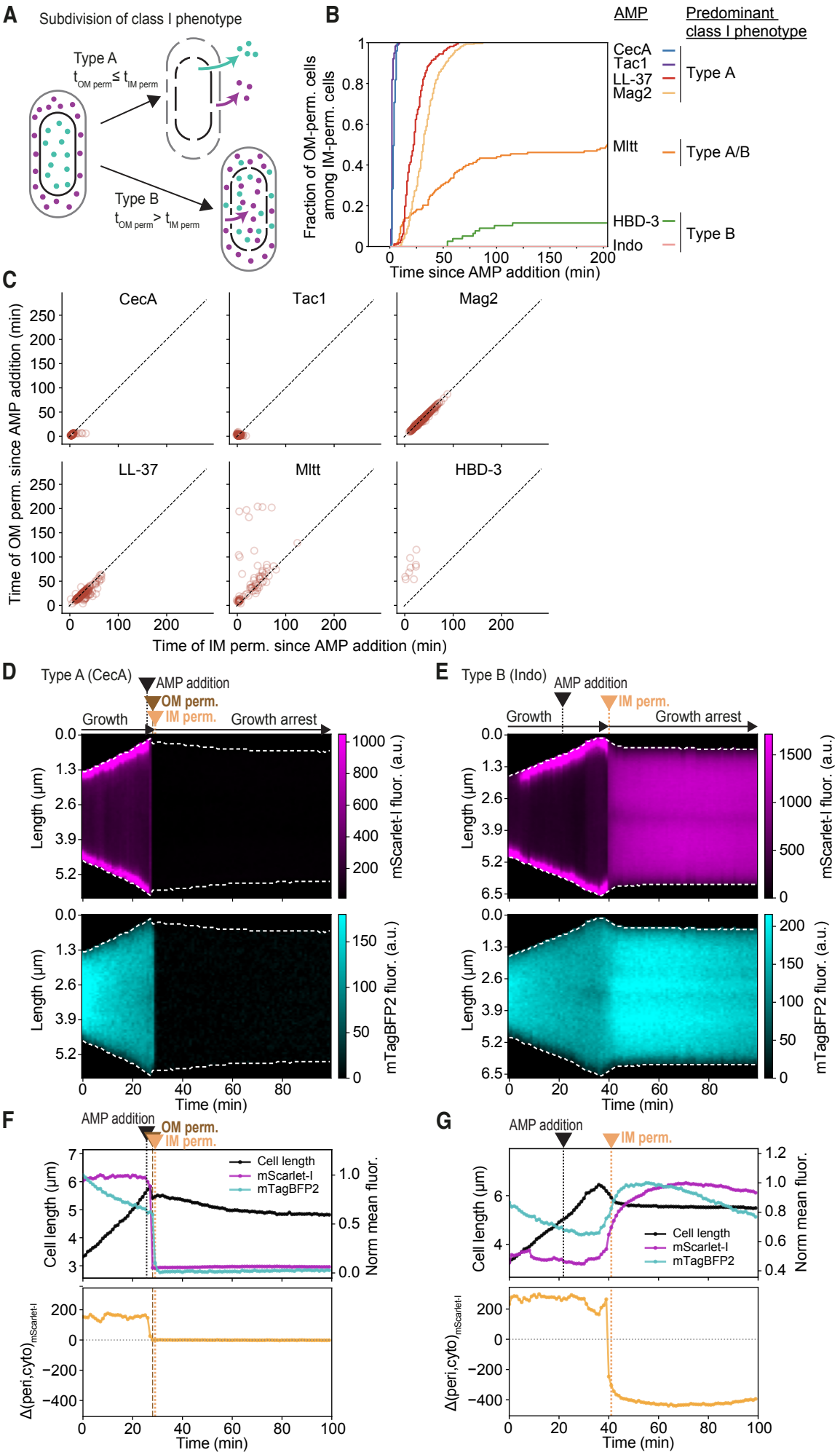
A
Subdivision of class I phenotype
Type A
$t_{OM\ perm} \leq t_{IM\ perm}$
Type B
$t_{OM\ perm} > t_{IM\ perm}$
B
AMP
Predominant class I phenotype
CecA
Tac1
LL-37
Mag2
Type A
MItt
Type A/B
HBD-3
Indo
Type B
Fraction of OM-perm. cells among IM-perm. cells
Time since AMP addition (min)
C
CecA
Tac1
Mag2
LL-37
MItt
HBD-3
Time of OM perm. since AMP addition (min)
Time of IM perm. since AMP addition (min)
D
Type A (CecA)
AMP addition
OM perm.
IM perm.
Growth
Growth arrest
Length (µm)
mScarlet-I fluor. (a.u.)
mTagBFP2 fluor. (a.u.)
Time (min)
E
Type B (Indo)
AMP addition
IM perm.
Growth
Growth arrest
Length (µm)
mScarlet-I fluor. (a.u.)
mTagBFP2 fluor. (a.u.)
Time (min)
F
AMP addition
OM perm.
IM perm.
Cell length
mScarlet-I
mTagBFP2
Cell length (µm)
Norm mean fluor.
$\Delta(peri,cyto)_{mScarlet-I}$
Time (min)
G
AMP addition
IM perm.
Cell length
mScarlet-I
mTagBFP2
Cell length (µm)
Norm mean fluor.
$\Delta(peri,cyto)_{mScarlet-I}$
Time (min)

Figure 3

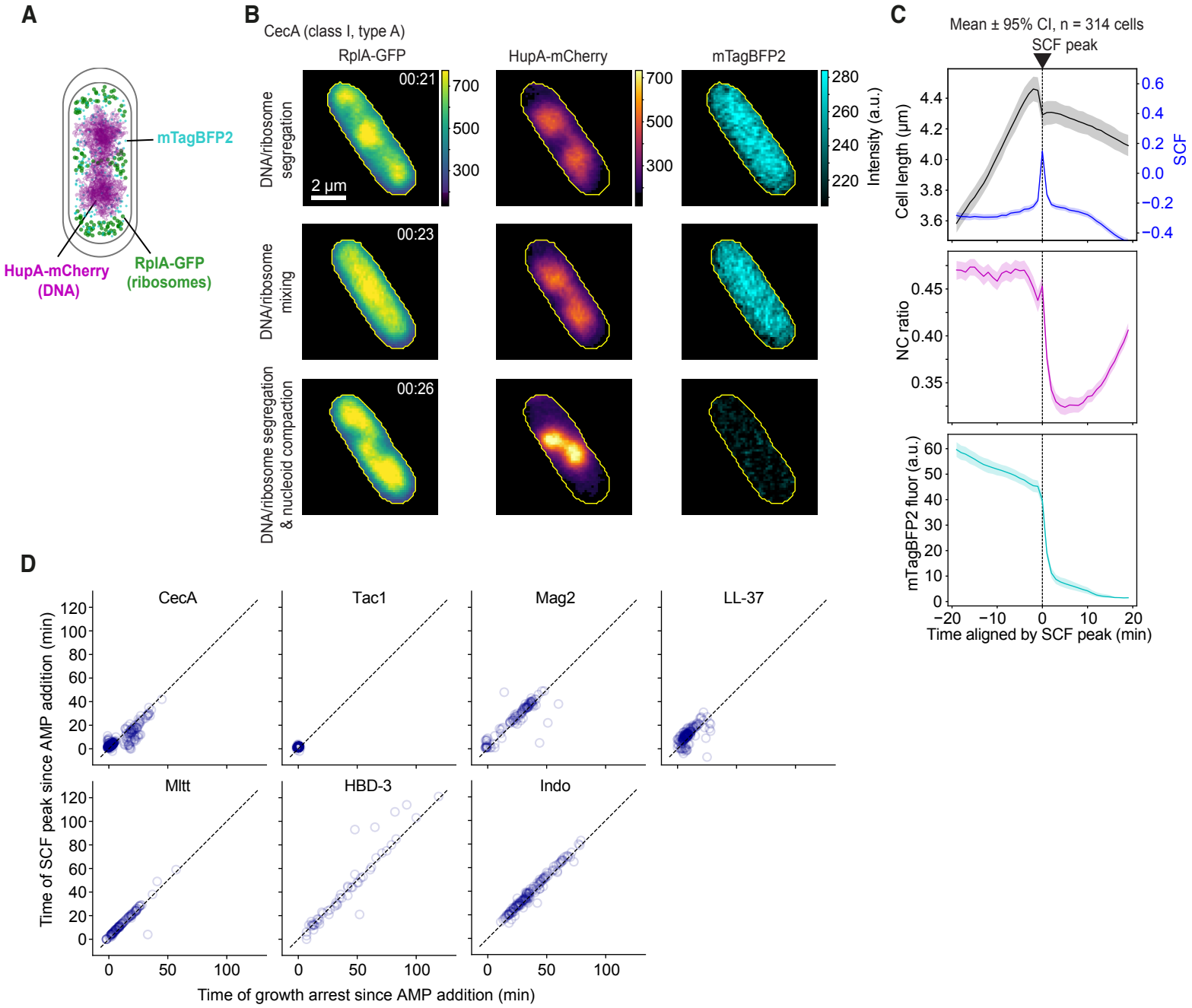
A
mTagBFP2
HupA-mCherry (DNA)
RplA-GFP (ribosomes)
B
CecA (class I, type A)
RplA-GFP
HupA-mCherry
mTagBFP2
DNA/ribosome segregation
DNA/ribosome mixing
DNA/ribosome segregation & nucleoid compaction
00:21
00:23
00:26
2 µm
Intensity (a.u.)
C
Mean ± 95% CI, n = 314 cells
SCF peak
Cell length (µm)
SCF
NC ratio
mTagBFP2 fluor (a.u.)
Time aligned by SCF peak (min)
D
CecA
Tac1
Mag2
LL-37
Mltt
HBD-3
Indo
Time of SCF peak since AMP addition (min)
Time of growth arrest since AMP addition (min)

Figure 4

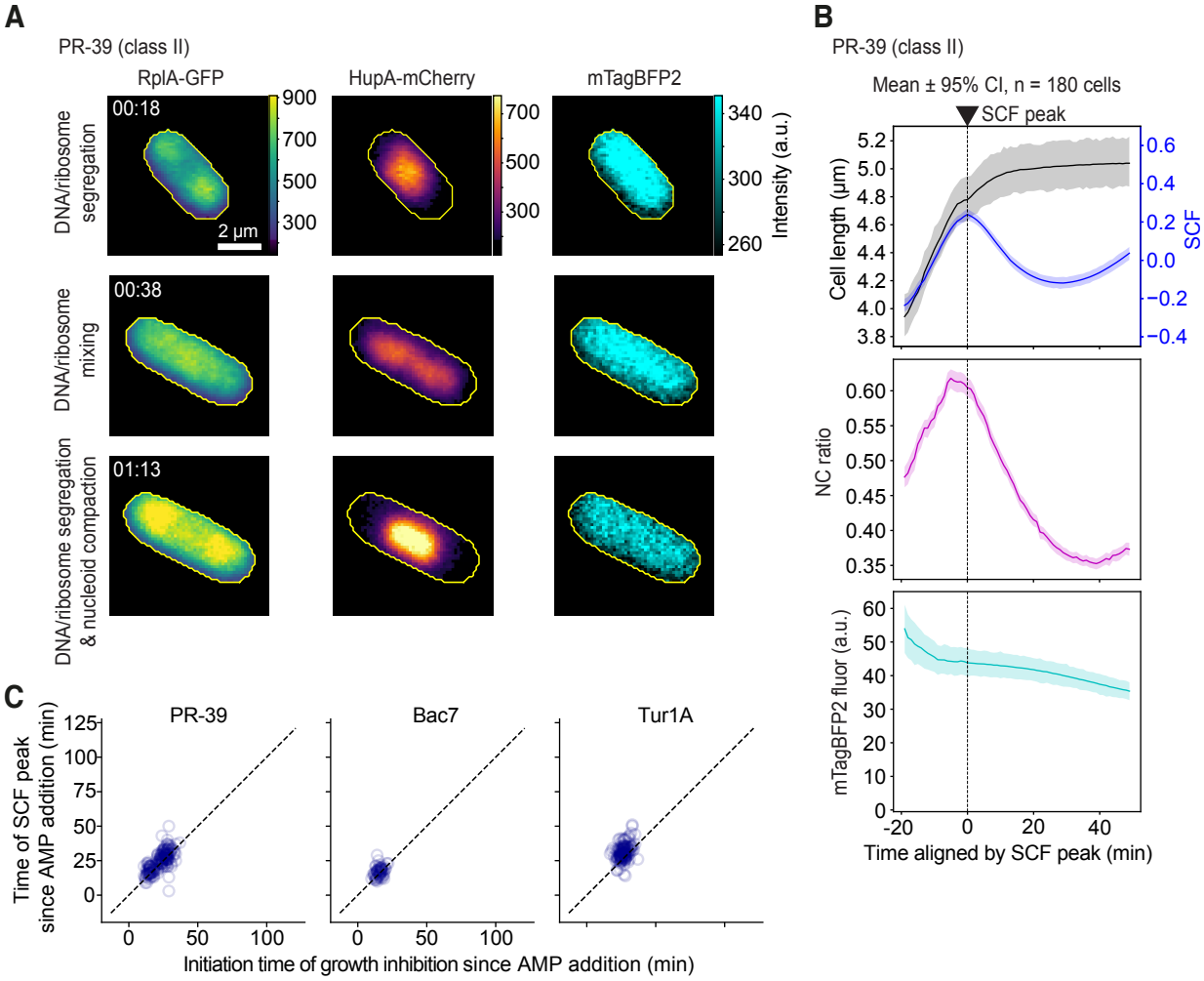
A
PR-39 (class II)
RplA-GFP
HupA-mCherry
mTagBFP2
DNA/ribosome segregation
DNA/ribosome mixing
DNA/ribosome segregation & nucleoid compaction
00:18
00:38
01:13
2 µm
900
700
500
300
340
260
Intensity (a.u.)
B
PR-39 (class II)
Mean ± 95% CI, n = 180 cells
SCF peak
Cell length (µm)
SCF
NC ratio
mTagBFP2 fluor (a.u.)
Time aligned by SCF peak (min)
C
PR-39
Bac7
Tur1A
Time of SCF peak since AMP addition (min)
Initiation time of growth inhibition since AMP addition (min)

Figure 5

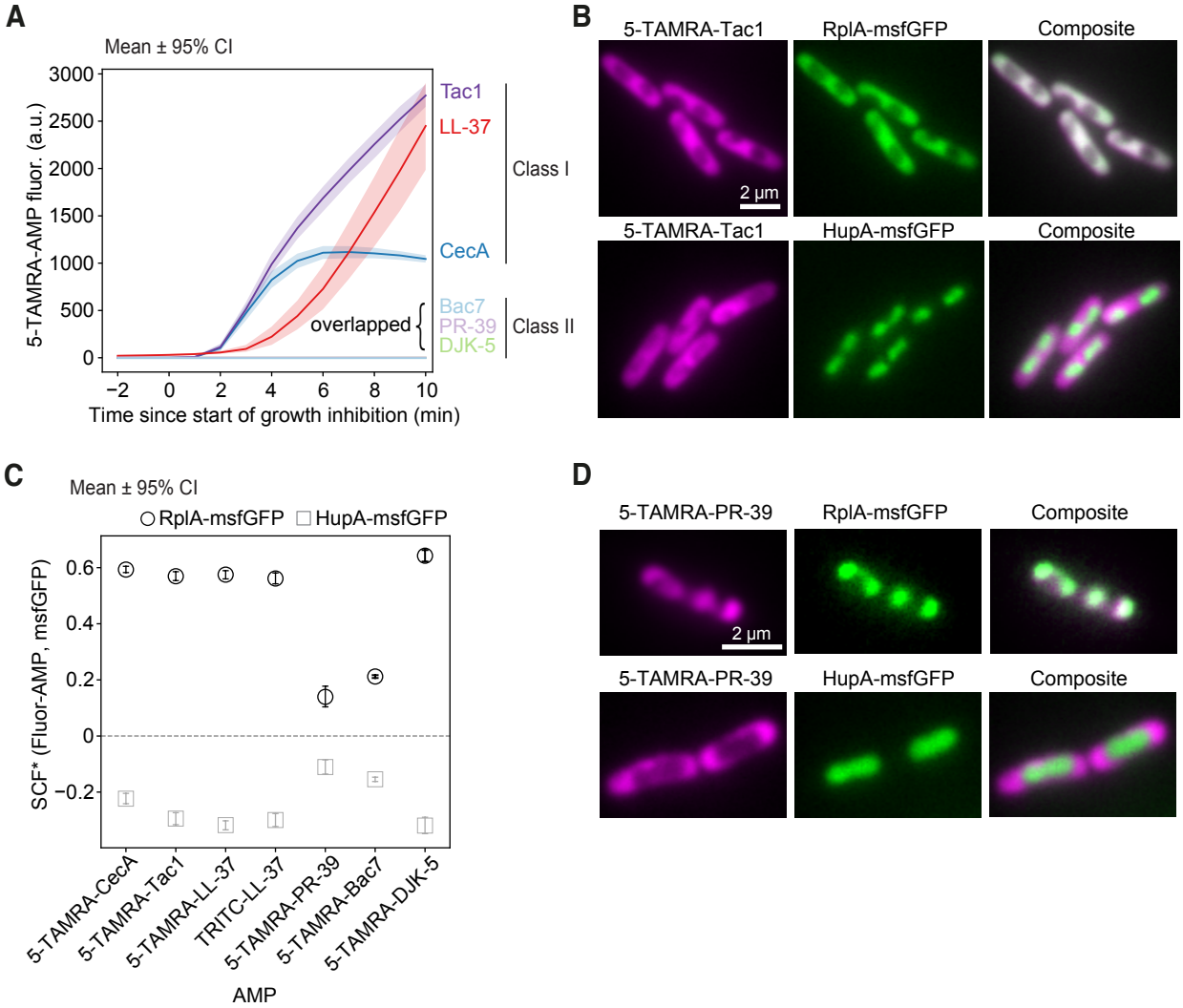
A
Mean ± 95% CI
5-TAMRA-AMP fluor. (a.u.)
3000
2500
2000
1500
1000
500
0
−2
0
2
4
6
8
10
Time since start of growth inhibition (min)
Tac1
LL-37
CecA
Bac7
PR-39
DJK-5
overlapped
Class I
Class II
B
5-TAMRA-Tac1
RplA-msfGFP
Composite
2 µm
5-TAMRA-Tac1
HupA-msfGFP
Composite
C
Mean ± 95% CI
RplA-msfGFP
HupA-msfGFP
SCF* (Fluor-AMP, msfGFP)
0.6
0.4
0.2
0
−0.2
5-TAMRA-CecA
5-TAMRA-Tac1
5-TAMRA-LL-37
TRITC-LL-37
5-TAMRA-PR-39
5-TAMRA-Bac7
5-TAMRA-DJK-5
AMP
D
5-TAMRA-PR-39
RplA-msfGFP
Composite
2 µm
5-TAMRA-PR-39
HupA-msfGFP
Composite

Figure 6

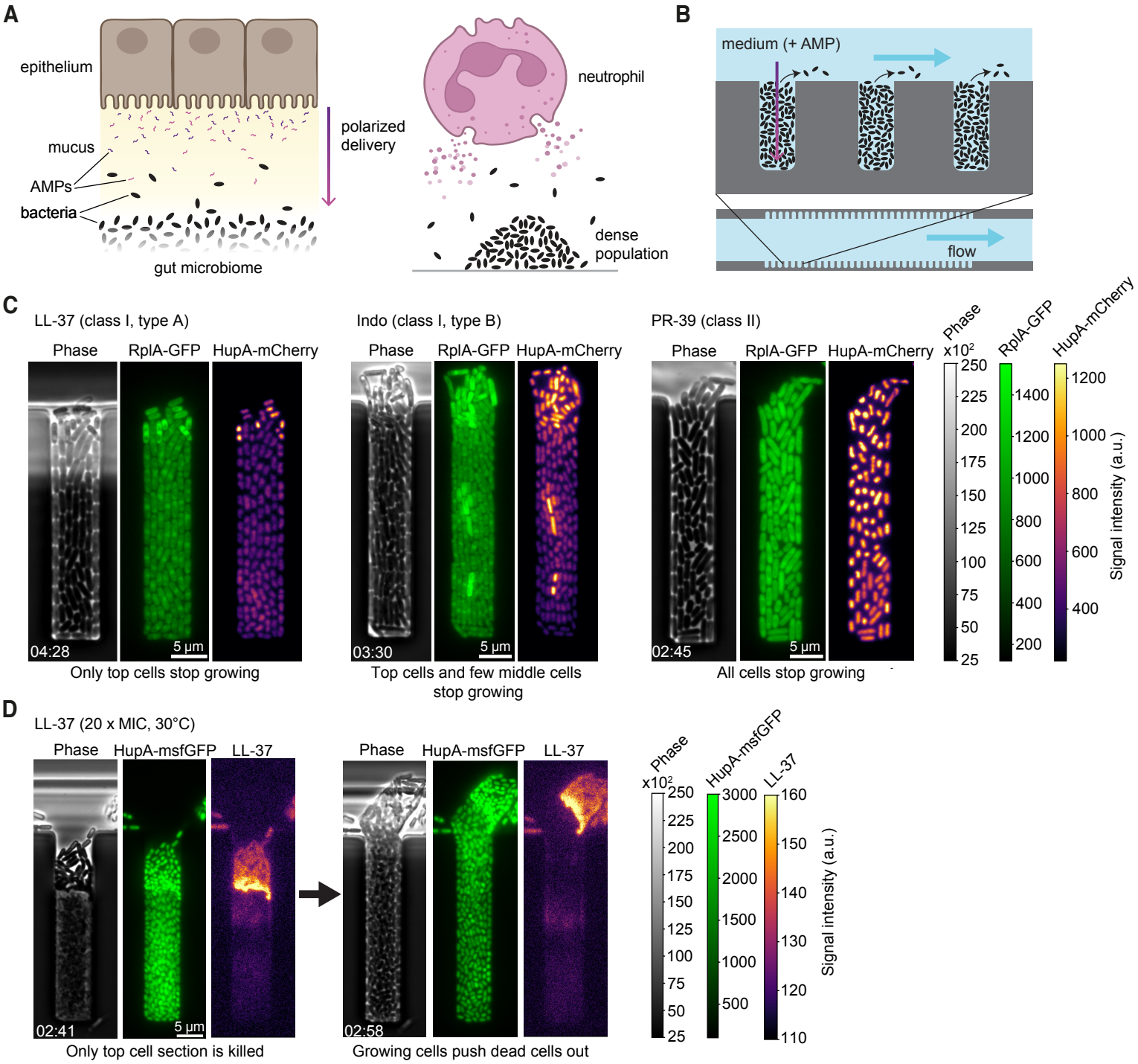
A
epithelium
mucus
AMPs
bacteria
gut microbiome
polarized delivery
neutrophil
dense population
B
medium (+ AMP)
flow
C
LL-37 (class I, type A)
Phase
RplA-GFP
HupA-mCherry
04:28
5 µm
Only top cells stop growing
Indo (class I, type B)
03:30
Top cells and few middle cells stop growing
PR-39 (class II)
02:45
All cells stop growing
Signal intensity (a.u.)
D
LL-37 (20 x MIC, 30°C)
HupA-msfGFP
LL-37
02:41
Only top cell section is killed
02:58
Growing cells push dead cells out

Figure 7

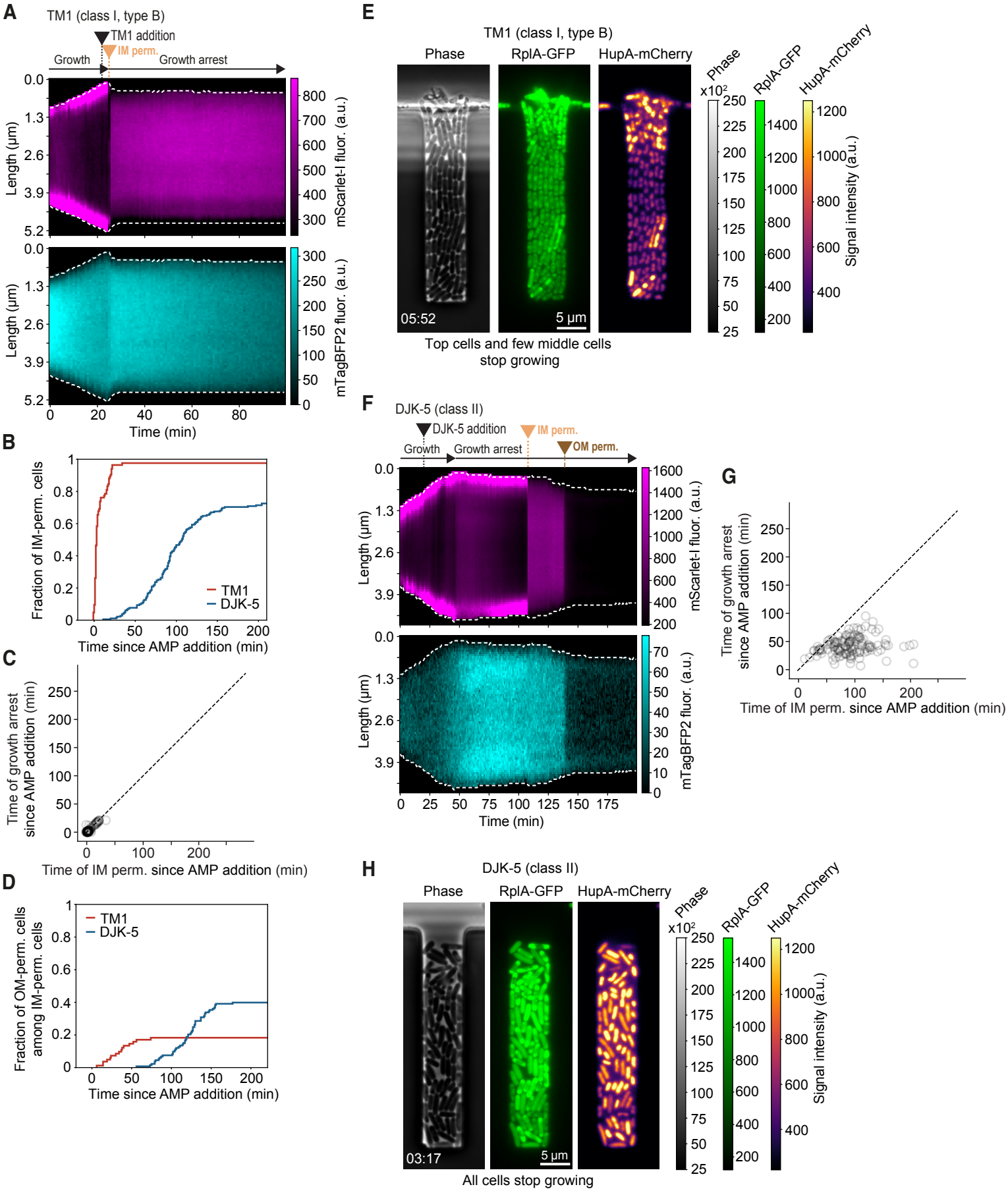
A
TM1 (class I, type B)
TM1 addition
IM perm.
Growth
Growth arrest
Length (μm)
mScarlet-I fluor. (a.u.)
mTagBFP2 fluor. (a.u.)
Time (min)
B
Fraction of IM-perm. cells
TM1
DJK-5
Time since AMP addition (min)
C
Time of growth arrest since AMP addition (min)
Time of IM perm. since AMP addition (min)
D
Fraction of OM-perm. cells among IM-perm. cells
TM1
DJK-5
Time since AMP addition (min)
E
TM1 (class I, type B)
Phase
RplA-GFP
HupA-mCherry
05:52
5 μm
Signal intensity (a.u.)
Top cells and few middle cells stop growing
F
DJK-5 (class II)
DJK-5 addition
IM perm.
OM perm.
Growth
Growth arrest
Length (μm)
mScarlet-I fluor. (a.u.)
mTagBFP2 fluor. (a.u.)
Time (min)
G
Time of growth arrest since AMP addition (min)
Time of IM perm. since AMP addition (min)
H
DJK-5 (class II)
Phase
RplA-GFP
HupA-mCherry
03:17
5 μm
Signal intensity (a.u.)
All cells stop growing

Figure S1

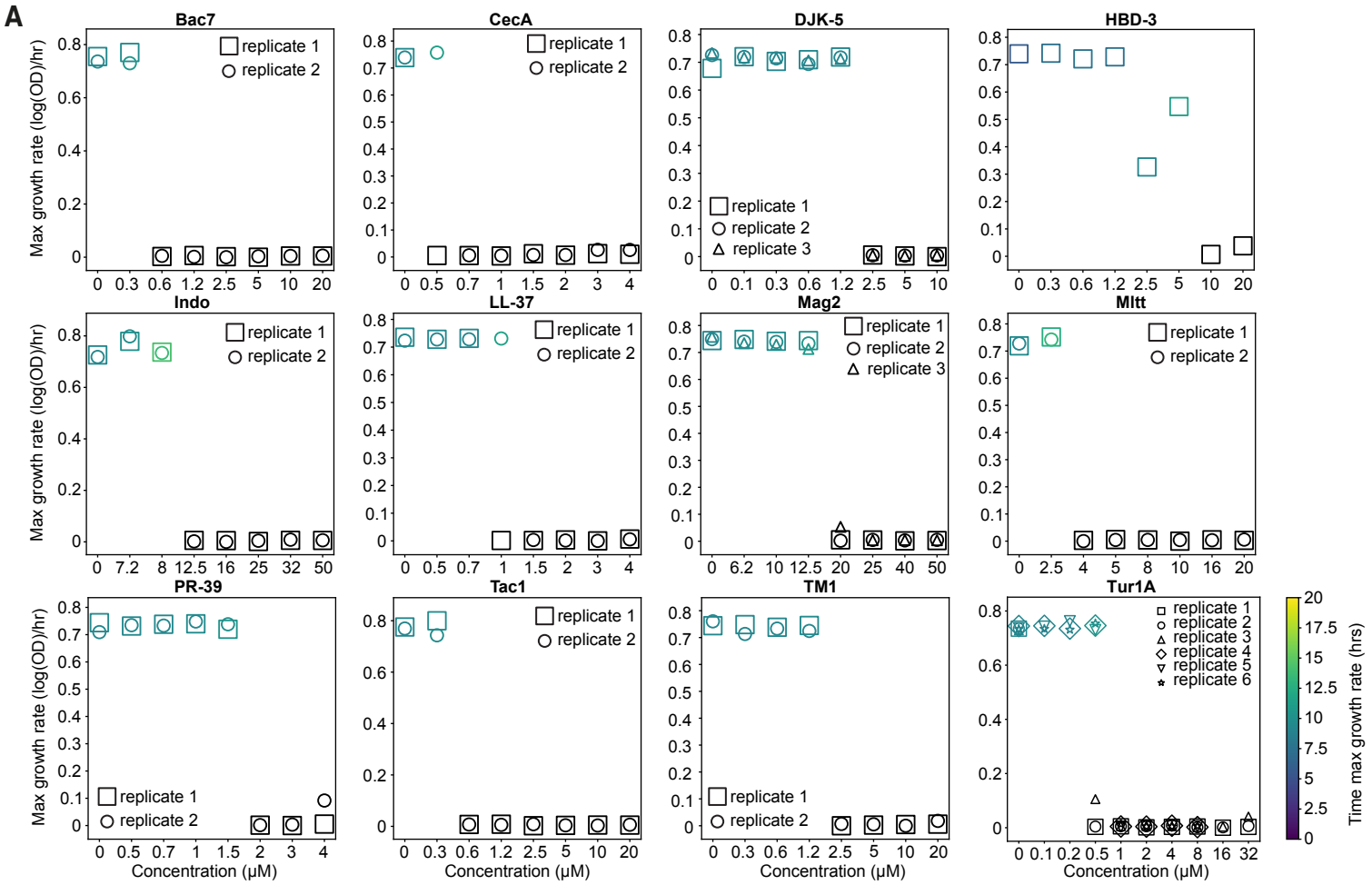
A
Bac7
CecA
DJK-5
HBD-3
Indo
LL-37
Mag2
MItt
PR-39
Tac1
TM1
Tur1A
Max growth rate (log(OD)/hr)
Concentration (μM)
Time max growth rate (hrs)
replicate 1
replicate 2
replicate 3
replicate 4
replicate 5
replicate 6

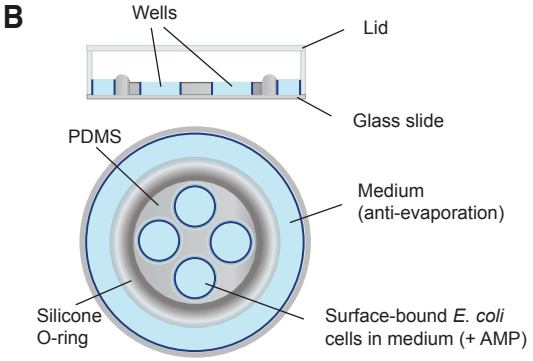
B
Wells
Lid
Glass slide
PDMS
Medium
(anti-evaporation)
Silicone
O-ring
Surface-bound E. coli
cells in medium (+ AMP)

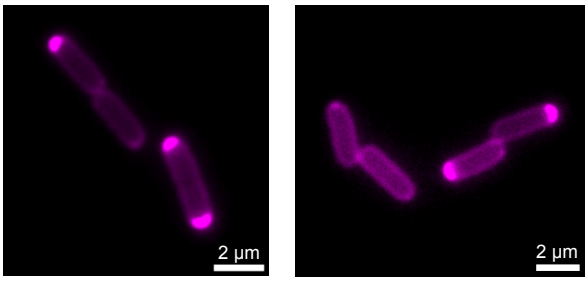
C
2 μm
2 μm

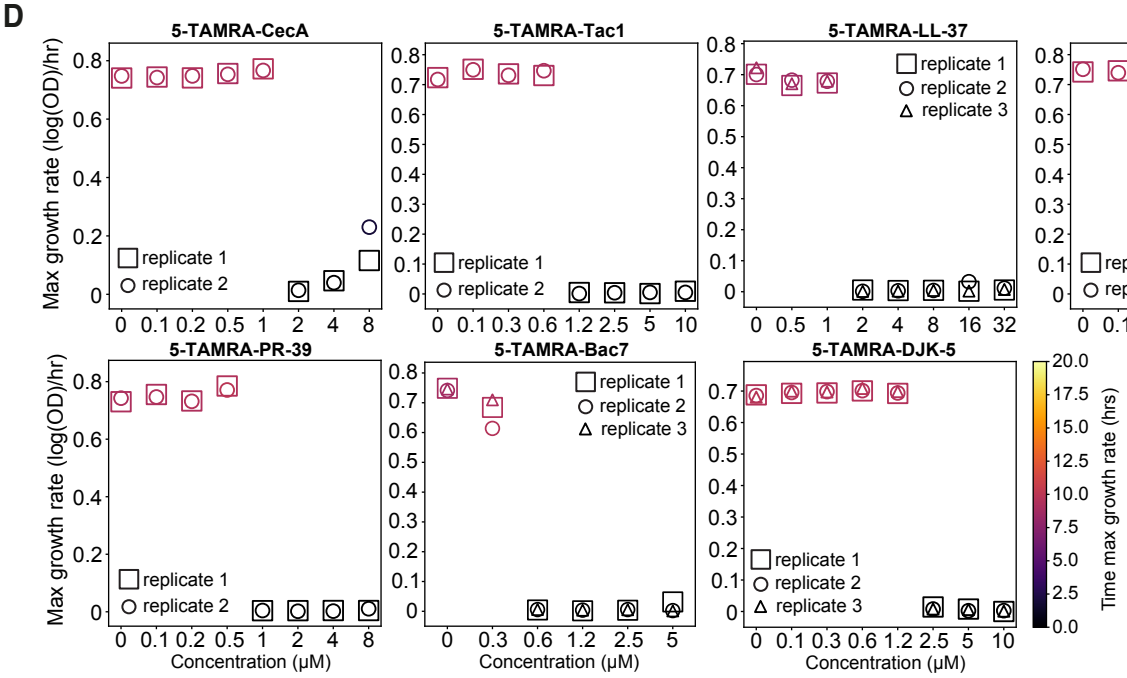
D
5-TAMRA-CecA
5-TAMRA-Tac1
5-TAMRA-LL-37
TRITC-LL-37
5-TAMRA-PR-39
5-TAMRA-Bac7
5-TAMRA-DJK-5
Max growth rate (log(OD)/hr)
Concentration (μM)
Time max growth rate (hrs)
replicate 1
replicate 2
replicate 3

Figure S2

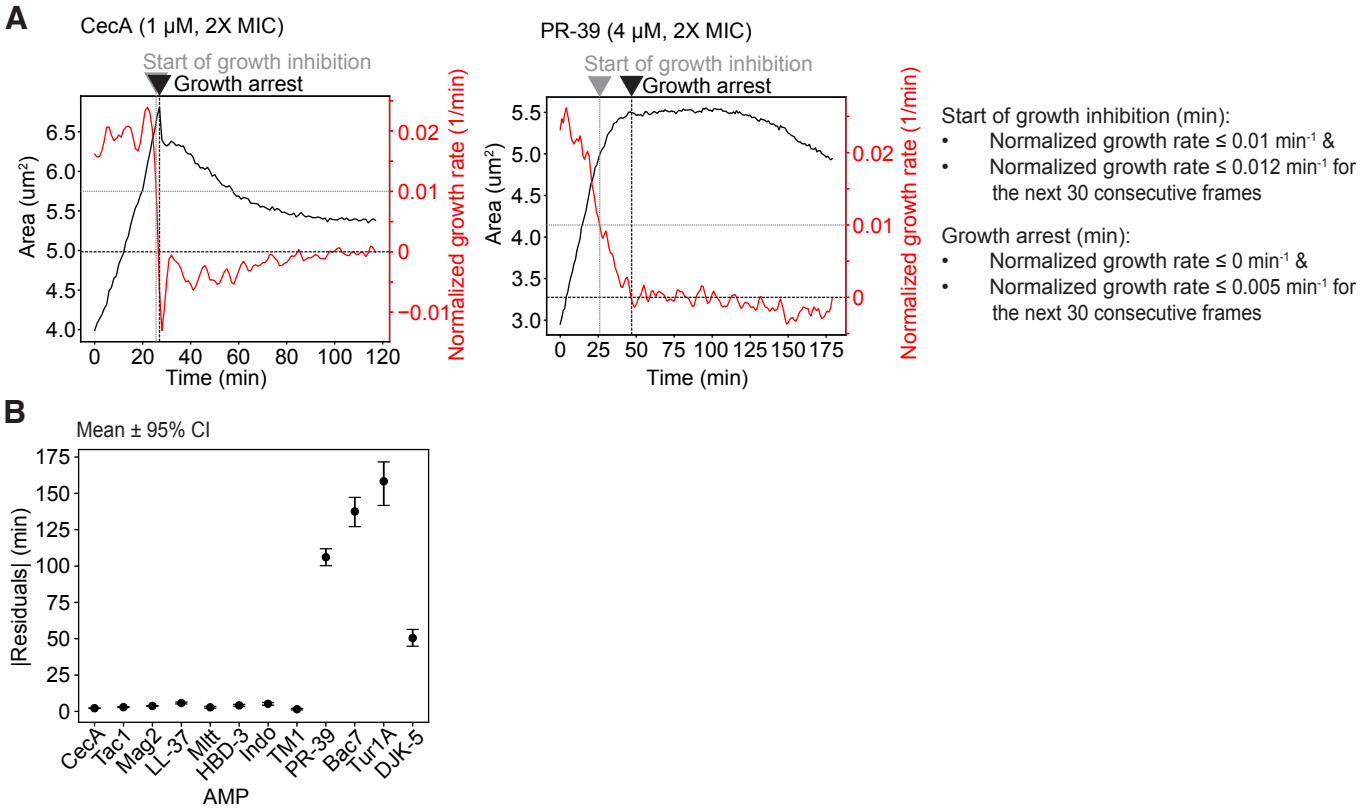
A
CecA (1 μM, 2X MIC)
Start of growth inhibition
Growth arrest
Area (um²)
Normalized growth rate (1/min)
Time (min)
PR-39 (4 μM, 2X MIC)
Start of growth inhibition
Growth arrest
Area (um²)
Normalized growth rate (1/min)
Time (min)
Start of growth inhibition (min):
• Normalized growth rate ≤ 0.01 min-1 &
• Normalized growth rate ≤ 0.012 min-1 for the next 30 consecutive frames
Growth arrest (min):
• Normalized growth rate ≤ 0 min-1 &
• Normalized growth rate ≤ 0.005 min-1 for the next 30 consecutive frames
B
Mean ± 95% CI
|Residuals| (min)
CecA
Tac1
Mag2
LL-37
Mltt
HBD-3
Indo
TM1
PR-39
Bac7
Tur1A
DJK-5
AMP

Figure S3

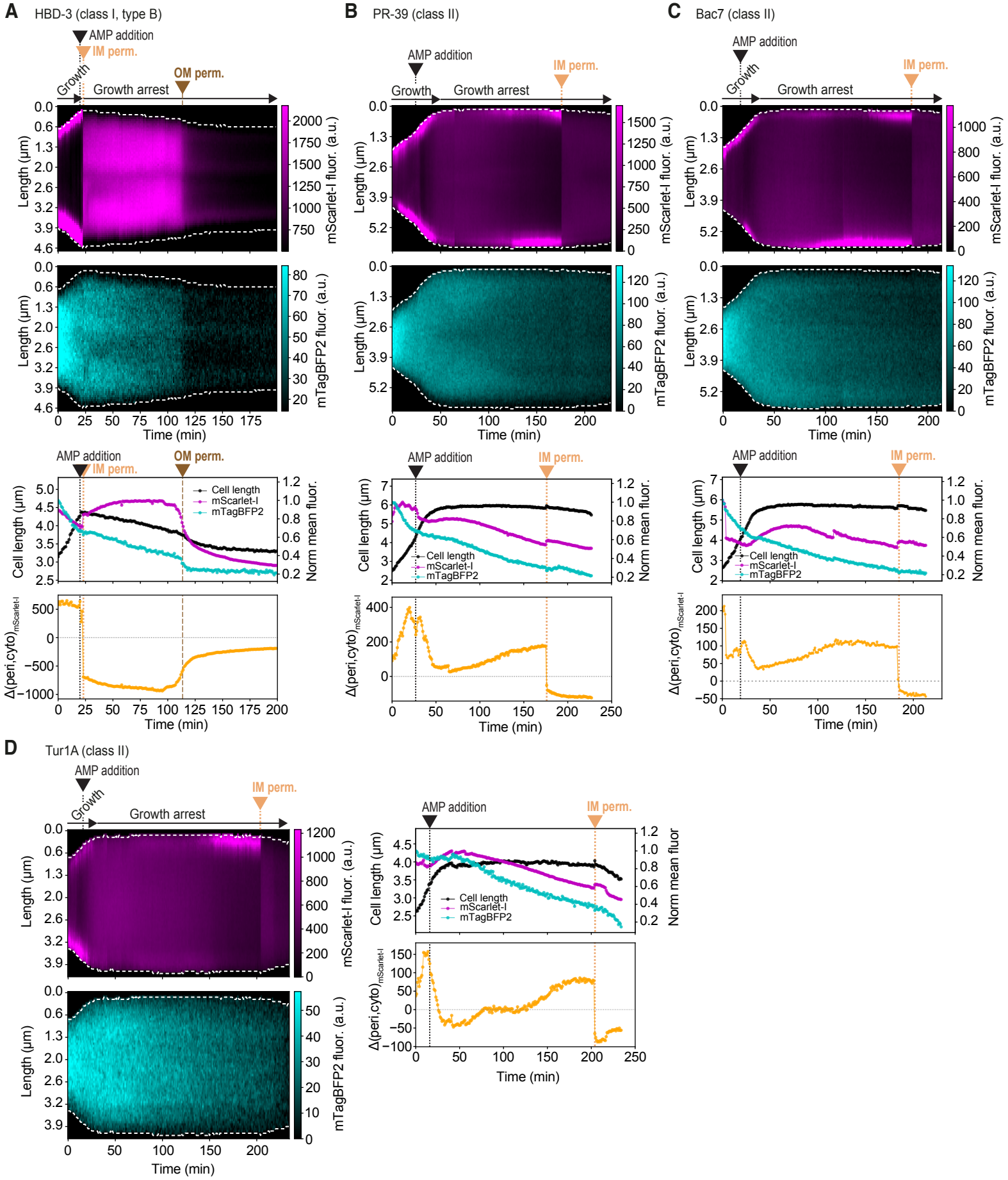
A
HBD-3 (class I, type B)
AMP addition
IM perm.
OM perm.
Growth
Growth arrest
Length (µm)
mScarlet-I fluor. (a.u.)
mTagBFP2 fluor. (a.u.)
Time (min)
Cell length
mScarlet-I
mTagBFP2
Norm mean fluor.
Δ(peri,cyto)mScarlet-I
B
PR-39 (class II)
C
Bac7 (class II)
D
Tur1A (class II)

Figure S4

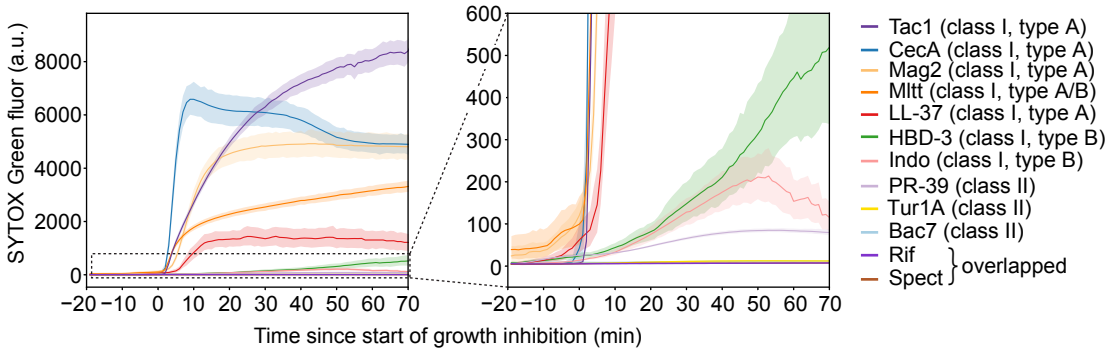
SYTOX Green fluor (a.u.)
8000
6000
4000
2000
0
600
500
400
300
200
100
0
−20 −10 0 10 20 30 40 50 60 70
Time since start of growth inhibition (min)
Tac1 (class I, type A)
CecA (class I, type A)
Mag2 (class I, type A)
Mltt (class I, type A/B)
LL-37 (class I, type A)
HBD-3 (class I, type B)
Indo (class I, type B)
PR-39 (class II)
Tur1A (class II)
Bac7 (class II)
Rif
Spect
overlapped

Figure S5

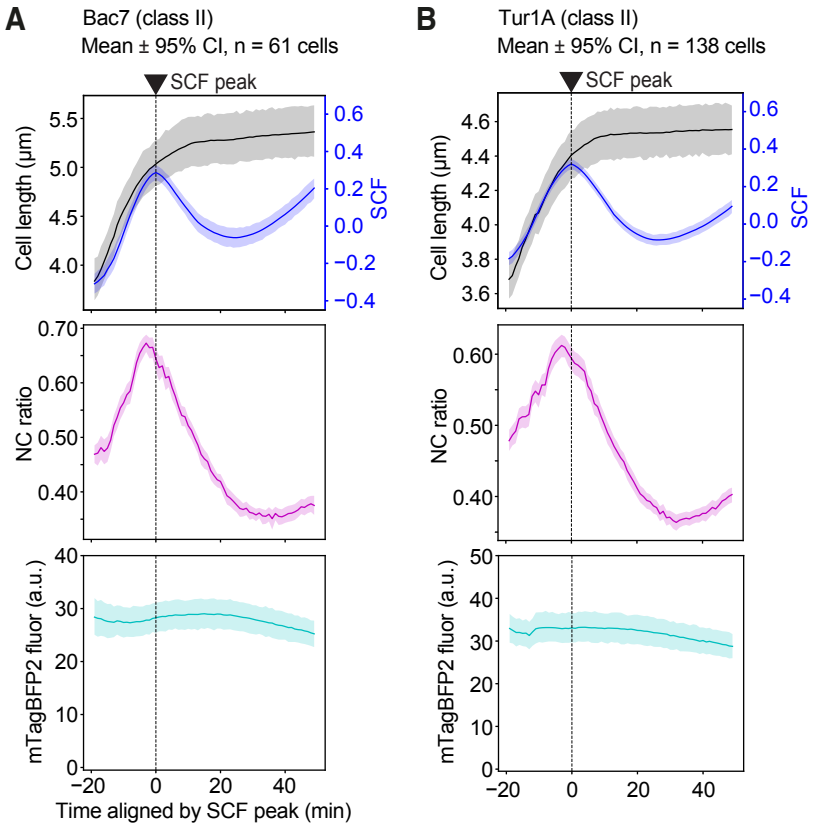
A
Bac7 (class II)
Mean ± 95% CI, n = 61 cells
SCF peak
Cell length (μm)
SCF
NC ratio
mTagBFP2 fluor (a.u.)
Time aligned by SCF peak (min)
B
Tur1A (class II)
Mean ± 95% CI, n = 138 cells
SCF peak
Cell length (μm)
SCF
NC ratio
mTagBFP2 fluor (a.u.)

Figure S6

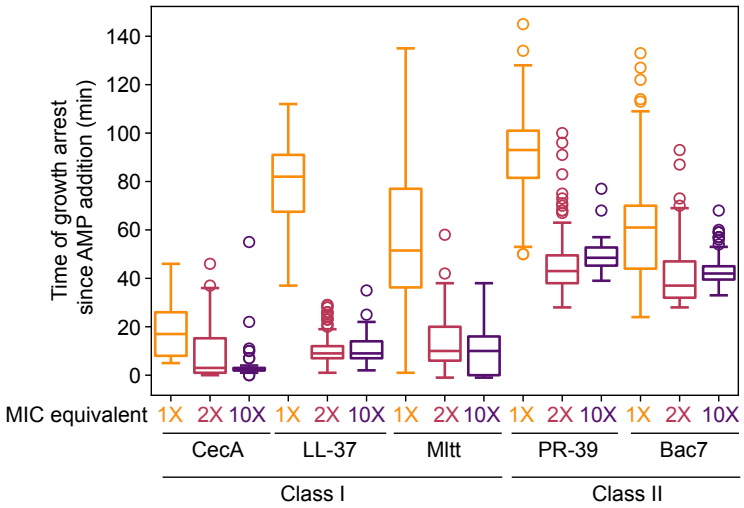
Time of growth arrest since AMP addition (min)
140
120
100
80
60
40
20
0
MIC equivalent
1X 2X 10X 1X 2X 10X 1X 2X 10X 1X 2X 10X 1X 2X 10X
CecA
LL-37
MItt
PR-39
Bac7
Class I
Class II

Figure S7

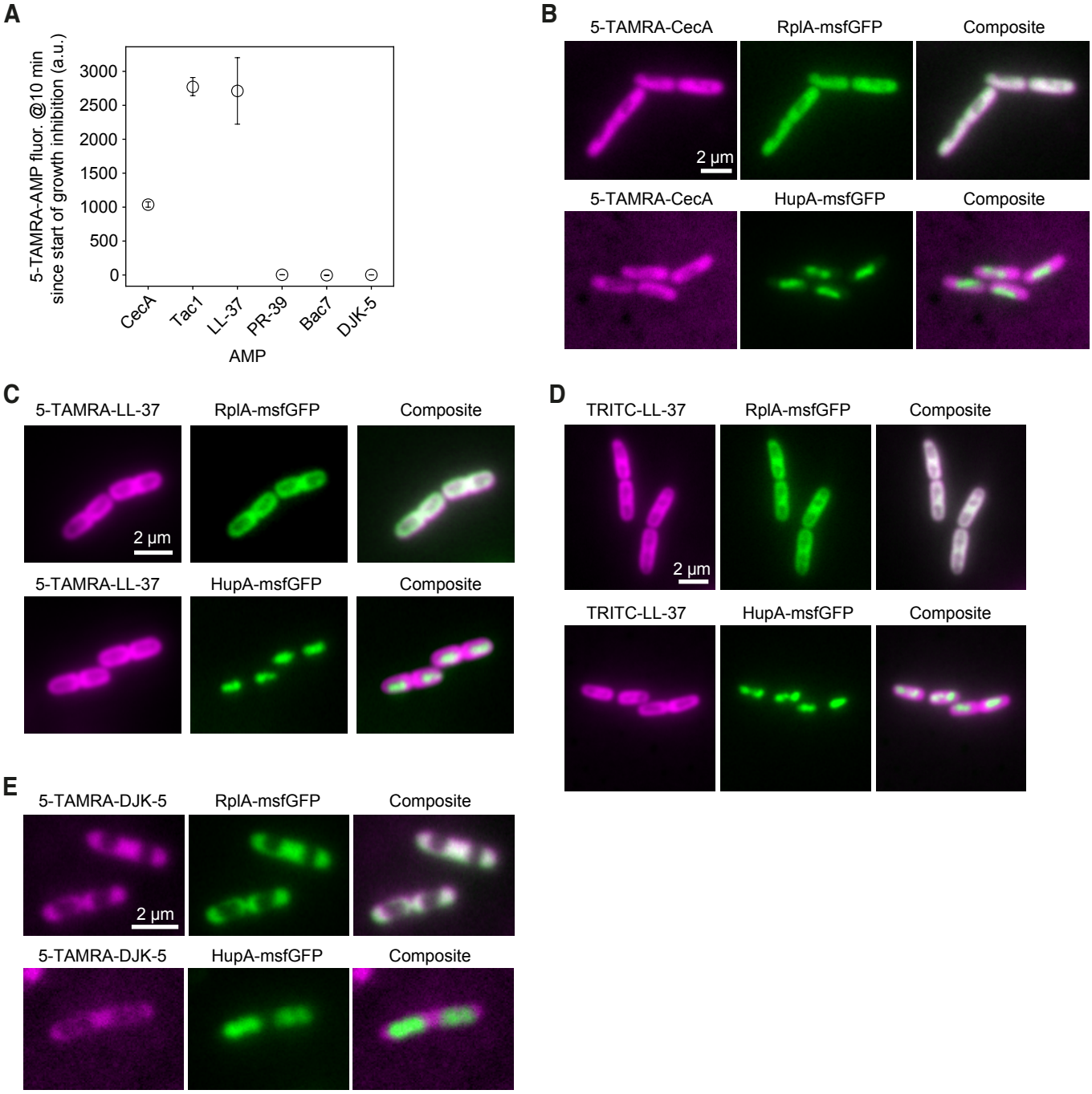
A
5-TAMRA-AMP fluor. @10 min since start of growth inhibition (a.u.)
3000
2500
2000
1500
1000
500
0
CecA
Tac1
LL-37
PR-39
Bac7
DJK-5
AMP
B
5-TAMRA-CecA
RplA-msfGFP
Composite
2 µm
5-TAMRA-CecA
HupA-msfGFP
Composite
C
5-TAMRA-LL-37
RplA-msfGFP
Composite
2 µm
5-TAMRA-LL-37
HupA-msfGFP
Composite
D
TRITC-LL-37
RplA-msfGFP
Composite
2 µm
TRITC-LL-37
HupA-msfGFP
Composite
E
5-TAMRA-DJK-5
RplA-msfGFP
Composite
2 µm
5-TAMRA-DJK-5
HupA-msfGFP
Composite

Figure S8

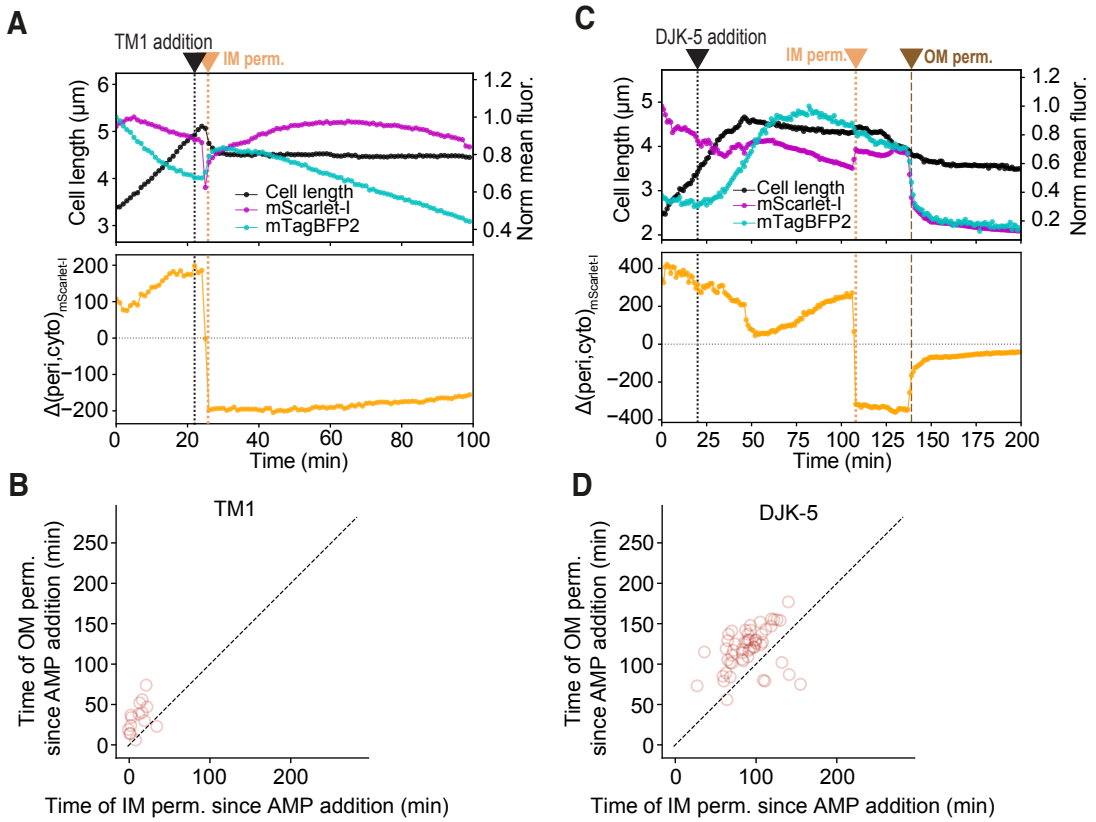
A
TM1 addition
IM perm.
Cell length (µm)
Norm mean fluor.
Cell length
mScarlet-I
mTagBFP2
Δ(peri,cyto)mScarlet-I
Time (min)
C
DJK-5 addition
IM perm.
OM perm.
Cell length (µm)
Norm mean fluor.
Cell length
mScarlet-I
mTagBFP2
Δ(peri,cyto)mScarlet-I
Time (min)
B
TM1
Time of OM perm. since AMP addition (min)
Time of IM perm. since AMP addition (min)
D
DJK-5
Time of OM perm. since AMP addition (min)
Time of IM perm. since AMP addition (min)

Table S1

Name (abbreviation)	Molecular weight (kDa)	Net charge	Lysine fraction	Arginine fraction	Gravy index	Proline fraction	Hydrophobic fraction	Polar fraction
Bactenecin-7 (Bac7)	4.21	11	0.0	0.31	-1.41	0.46	0.2	0.8
Cecropin A (CecA)	4.0	7	0.19	0.03	-0.07	0.03	0.46	0.54
DJK-5	1.55	5	0.0	0.33	0.08	0.0	0.58	0.42
Human beta-defensin 3 (HBD-3)	5.16	11	0.13	0.16	-0.7	0.02	0.33	0.67
Indolicidin (Indo)	1.91	4	0.08	0.15	-1.07	0.23	0.54	0.46
LL-37	4.49	6	0.16	0.14	-0.72	0.03	0.35	0.65
Magainin-2 (Mag2)	2.47	3	0.17	0.0	0.08	0.0	0.43	0.57
Melittin (Mltt)	2.85	6	0.12	0.08	0.27	0.04	0.46	0.54
PR-39	4.72	11	0.0	0.26	-1.31	0.49	0.21	0.79
Tachyplesin-1 (Tac1)	2.26	7	0.06	0.29	-0.52	0.0	0.47	0.53
Tur1A	3.97	10	0.0	0.31	-1.12	0.38	0.25	0.75